FULLY-IMPLANTABLE SELF-CONTAINED DUAL-CHANNEL ELECTRICAL RECORDING AND DIRECTIVITY-ENHANCED OPTICAL STIMULATION SYSTEM ON A CHIP

TAYEBEH YOUSEFI

A THESIS SUBMITTED TO
THE FACULTY OF GRADUATE STUDIES
IN PARTIAL FULFILLMENT OF THE REQUIREMENTS
FOR THE DEGREE OF
MASTER OF COMPUTER SCIENCE AND ELECTRICAL ENGINEERING

GRADUATE PROGRAMME IN COMPUTER SCIENCE AND
ELECTRICAL ENGINEERING
YORK UNIVERSITY
TORONTO, ONTARIO

AUGUST 2019

ABSTRACT

This thesis presents an integrated system-on-a-chip (SoC), designed, fabricated, and characterized for conducting simultaneous dual-channel optogenetic stimulation and electrophysiological recording. An inductive coil as well as power management circuits are also integrated on the chip, enabling wireless power reception, hence, allowing full implantation.

The optical stimulation channels host a novel μLED driver circuit that can generate currents up to 10mA with a minimum required headroom voltage reported in the literature, resulting in a superior power efficiency compared to the state of the art. The output current in each channel can be programmed to have an arbitrary waveform with digitally-controlled magnitude and timing. The final design is fabricated as a 3×4 mm^2 microchip using a CMOS 130nm technology and characterized both in terms of electrical and optical performance.

A pair of custom-designed inkjet-printed micro-lenses are also fabricated and placed on top of the μLEDs. The lenses are optimized to enhance the light directivity of optical stimulation, resulting in significant improvements in terms of spatial resolution, power consumption (30.5x reduction), and safety aspects (temperature increase of <0.1ºc) of the device.

ACKNOWLEDGEMENTS

TABLE OF CONTENTS

Table of Contents

LIST OF TABLES

LIST OF FIGURES

x

Chapter 1

Introduction

1.1 Introduction to Optogenetics

Investigating the brain functions and dysfunctions to better understand and possibly treat neurological disorders such as Epilepsy and Parkinson not only requires tools/methods for continuous activity monitoring (e.g., electroencephalography), but also needs means for manipulating the neurons' activity. Pharmacological agents, magnetic stimulation and electrical stimulation are capable of altering brain neuronal activities [1], [2], [3]. These methods generally vary in terms of activation latency, level of invasiveness, spatial and temporal precision, etc.

Optogenetics is a relatively new method for brain electro-physiological activity modulation that has received significant attention over the past decade [4], mainly due to single-cell-scale spatial resolution and millisecond-scale temporal precision [5]. Optogenetic stimulation is performed by first, introducing light-sensitive proteins to the

neuron membrane by genetically modifying the target neurons, and next, modulation of the neural activities using optical stimulation at a specific wavelength [6], [7].

This introductory chapter starts by explaining the mechanism of how introducing and optically stimulating such light-sensitive neurons could change inter-neuron signaling in the brain, followed by describing and comparing commonly-used types of light-sensitive proteins. Next, Optogenetic is compared with electrical stimulation, as one of the most commonly used methods of neurological modulation. Next, a conclusive literature review of the significant projects in this area is presented along with their advantages and shortcomings, which brings us to the objective of this work. The chapter ends with a summary of the thesis organization.

1.2 Action potential generation

To better describe the mechanism underlying the optogenetic stimulation, the generation procedure of a single action potential (the change in cell membrane's potential that plays a key role in cell-to-cell communications) should be explained. Action potential generation is a result of ion flow through the membrane of excitable cells such as neurons. Ion channels and ion pumps are two types of border guards that control the ion movements across the cell membrane by allowing specific ion cross passing the neuron membrane [8]. When ion channels open, movement of selected ions specific to that channel generates a current in the direction of electrical potential and concentration gradient. On the contrary, ion pumps consume energy to act against electrical potential and concentration gradient to

maintain the resting membrane potential by moving the ions in the opposite direction from the ion flow through the channels.

When the neuron is in the resting state, there is a voltage difference across the membrane due to the different ion concentrations between inside and outside of the cell. For a neuron in the resting, the Na+ ion concentration is higher in extracellular fluid, and K^+ ion concentration is higher in intracellular fluid, resulting in a resting potential of approximately -70mV. Figure 1.1 is a simple illustration of the cell membrane, showing the ion channels and pumps, as well as sodium and potassium ion concentrations during resting.
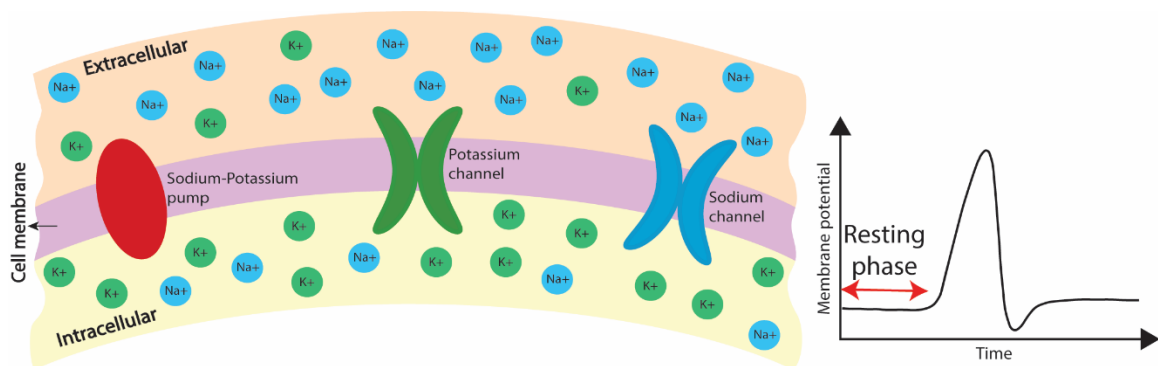
Figure 1.1: Resting membrane potential and ion concentration.

The main contributors to the generation of an action potential in a neuron are Na^+ and K^+ channels, both being controllable by membrane voltage (voltage-gated channels). These channels will open when the voltage across the neuron membrane reaches a certain magnitude, typically due to a triggering event or cross membrane ion movement. Figure 1.2 shows the *"Depolarization"* phase where the opening of Na^+ channels causes an inward

sodium ion flow, resulting in the neuron to be positively charged, hence an increase in the membrane potential.
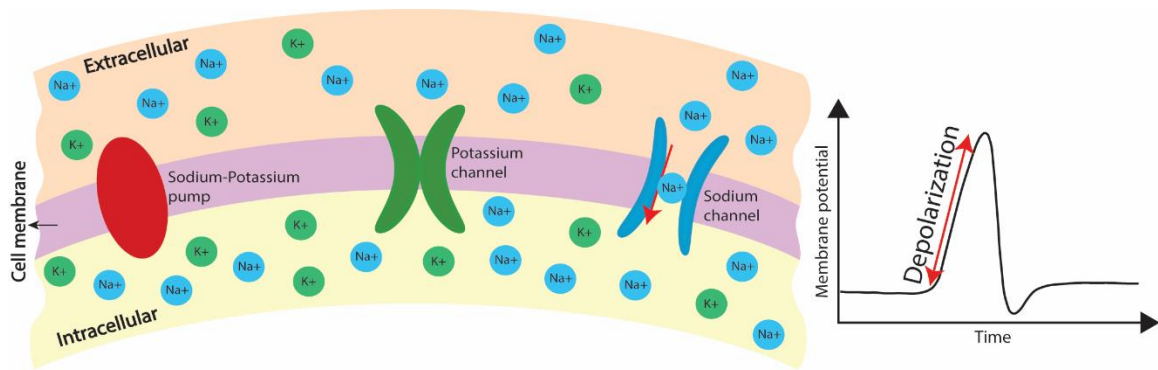
Figure 1.2: Depolarization phase of action potential generation.

The voltage increase due to the depolarization continues until the membrane potential is high enough to trigger the K+ channels to open and the Na+ channels to close. As shown in Figure 1.3 this means stopping the inward current of Na$^+$ ions, and simultaneously generating an outward flow of K$^+$ ions. *"Repolarizing"* the membrane voltage will continue even below the typical resting potential resulting in *"hyperpolarization"* phase.
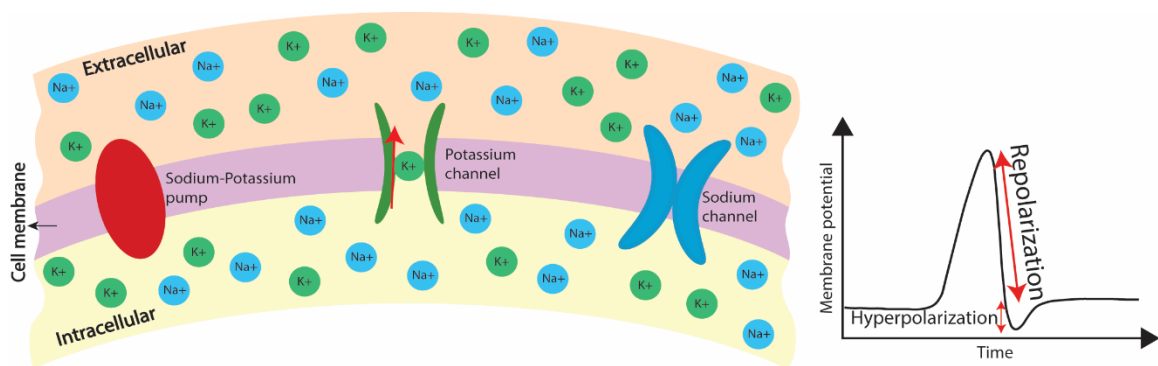
Figure 1.3: Repolarization phase of action potential generation.

Finally when hyperpolarization pushes the membrance voltage low enough to close the K+ channels, the sodium-potassium pumps will start to re-establish the ion concentration in intracellular and extracellular region, leading the neurons back to the resting state. As presented in Figure 1.4, since pumps are moving the ions against the electrical potential and concentration gradient, they need to consume energy in the form of adenosine triphosphate (ATP). Therefore, unlike the channels, this ion flow is not spontaneous after opening of ion pumps.
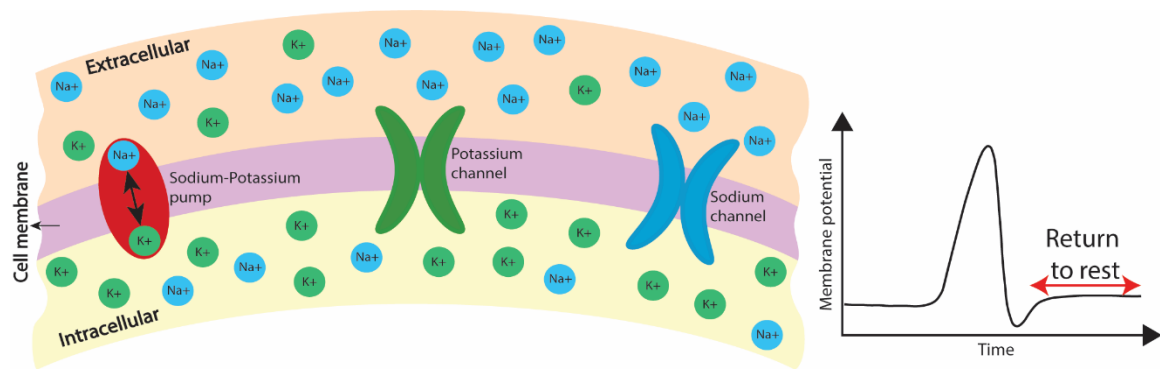
Figure 1.4: Ion pumps function to re-establish resting potential.

1.3 Light-sensitive neurons

As mentioned earlier, one way to manipulate the brain electrophysiological activity is through optogenetics. It involves introducing special proteins to the neuron membrane, called opsins that are sensitive to a specific optical wavelength. These proteins either form light-sensitive channels or pumps inside the cell membrane, or alter the membrane resting potential across the membrane. Light-sensitive ion channels and pumps allow for generation and abortion of action potentials, respectively, triggered by an incident light

with the right wavelength and sufficient energy. Altering the resting potential of the membrane can increase/decrease its excitability

There has been a great effort on the electrophysiology aspect of optogenetics to generate different types of opsins, each sensitive to a specific optical wavelength with different reactions (e.g., excitatory or inhibitory) to an incident light. Such variety helps with a more precise control of brain signaling mechanism. Table 1.1 lists the three types of opsins reported and used in literature, and their properties.

Table 1.1: Opsin comparison.

Opsin	Effect	Membrane structure	Activation wavelength	Required irradiance	Deactivation
ChR2	Excitatory	Channel	470 nm (Blue)	1-10 mW/mm^2	Illumination cessation
NpHR	Inhibitory	Pump	590 nm (Yellow)	3.5-10 mW/mm^2	Illumination cessation
SFO	Excitatory	Resting Potential	470 nm (Blue)	0.01-0.1 mW/mm^2	Green/Yellow light (2.4 mW/mm^2)

1.4 Optogenetic vs electrical stimulation

The neural stimulation mechanism described above results in a set of unique features for optogenetics compared to other neuro-modulation techniques (e.g., electrical, magnetic, etc.) that enable experimental studies that were impossible with conventional methods. As presented in Figure 1.5 the first advantage of optogenetics stimulation its cell-type specificity, which means unlike electrical stimulation that excites all the neurons in the

proximity of the electrode, only the neurons that are genetically-modified will be affected by the optical stimulation. The other important difference is, while optogenetics is capable of excitatory and inhibitory effects [9], inducing inhibitory effects using electrical stimulation is usually an indirect and power inefficient process [10]. Another big advantage of optogenetics is the possibility of simultaneous recording and stimulation. This is not the case for electrical stimulation as the stimulation pulses generate artifacts that are orders of magnitude larger than the signal of interest, causing amplifier saturation [11]. Moreover, optical stimulation does not carry the risk of tissue damage due to charge accumulation, while electrical stimulation requires charge-balancing auxiliary circuits to avoid such an issue. Table 1.2 summarizes the main features of optogenetic versus electrical stimulation.
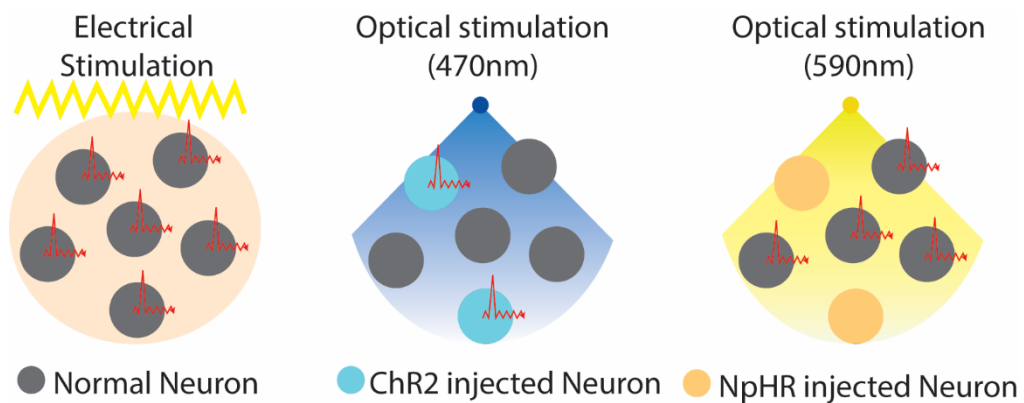
Figure 1.5: Optical stimulation versus electrical stimulation.

Table 1.2: Optogenetic vs electrical stimulation.

	Electrical Stimulation	Optogenetic Stimulation
Cell-type Specificity	No	Yes
Effects	Excitatory	Excitatory inhibitory
Charge Balance	Required	Not required
Simultaneous Rec. & Stim.	No	Yes
Require Direct Contact	No	Yes
Require Genetic Modification	No	Yes

1.5 Review of state-of-the-art

The unique advantages of optogenetics have motivated many researchers across various fields such as biology (e.g., studying various opsins), medicine (running clinical optogenetic experiments), and engineering (development and miniaturization of tools that enable optogenetic experiments). The engineering efforts range from efficiency-optimization of light-generating elements to the design and integration of electronic circuits for driving, controlling, and communicating with such light sources. In the rest of this section, a comparative review of the major state-of-the-art research efforts aimed at the design and development of optogenetic microsystems is presented.

A head-mountable device for simultaneous optical stimulation and electrical recording with wireless data transmission is presented in [12]. In this design, a mixed-signal controller is implemented to precisely control optical stimulation light intensity. However, this design requires a 3.7V Lithium-ion polymer battery as the power supply (16.0mm x 15.0mm x 5.0mm, 1.9gr) and a separate PCB for data transmission. Furthermore, since this system should be placed on the head it needs to use an optical fiber

going through the skull bone to deliver the light to the target tissue. As presented Figure 1.6, using the battery, discrete components for wireless data transmission and the optrode significantly limits the degree to which this device can be miniaturized. The LED-driver in this design uses a current mirror structure presented in [13] which is capable of generating a linearly controllable current to drive the LED.
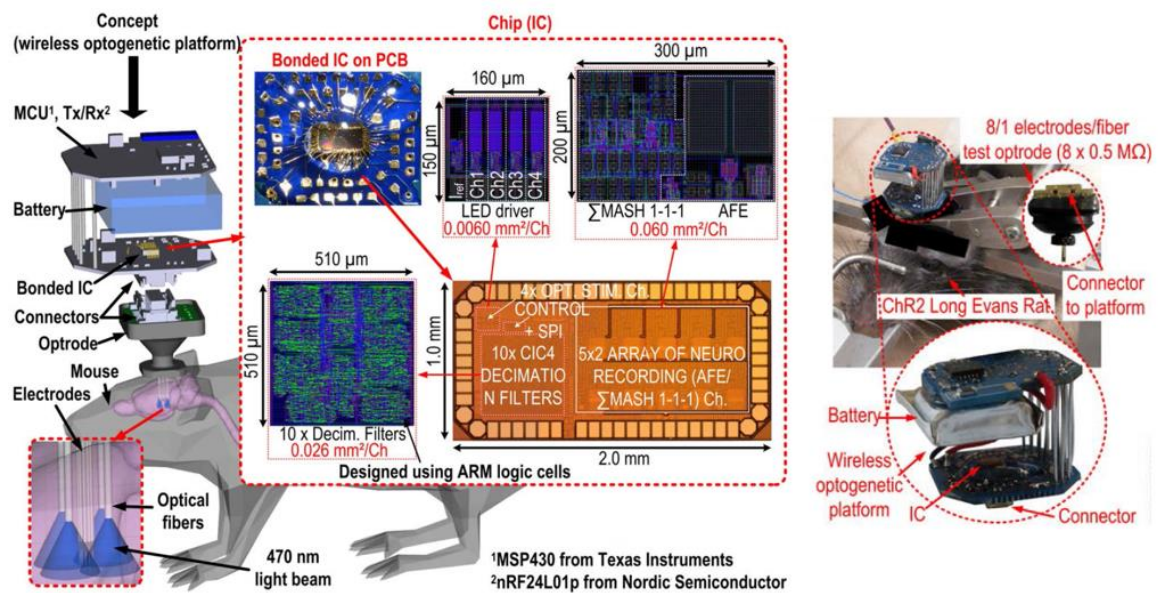
Figure 1.6: (Left) Die micrograph plus system level concept of the optogenetic device; (Right) Assembled version of the presented design in [12]**.**

Figure 1.7 and Figure 1.8 present two miniaturized fully-implantable wireless optogenetic stimulation systems reported in [14] and [15], respectively. Both systems are wirelessly powered and use μLEDs as their light source with off-the-shelf electronic components to implement the driving circuit. The discrete design prevents system scaling (in terms of channel count), and none of the two provides control on the light intensity.

Furthermore, both systems are stimulation only, and recording must be done with other equipment. In both of these designs, the LED optical power is solely controlled by the amount of delivered power from the inductive link.
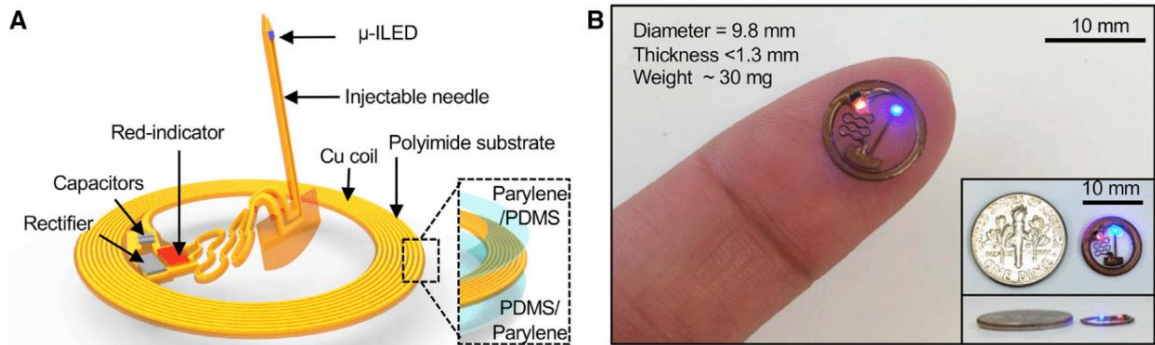
Figure 1.7: Thin, flexible wireless optoelectronic implant using discrete off-the-shelf components [14]**.**
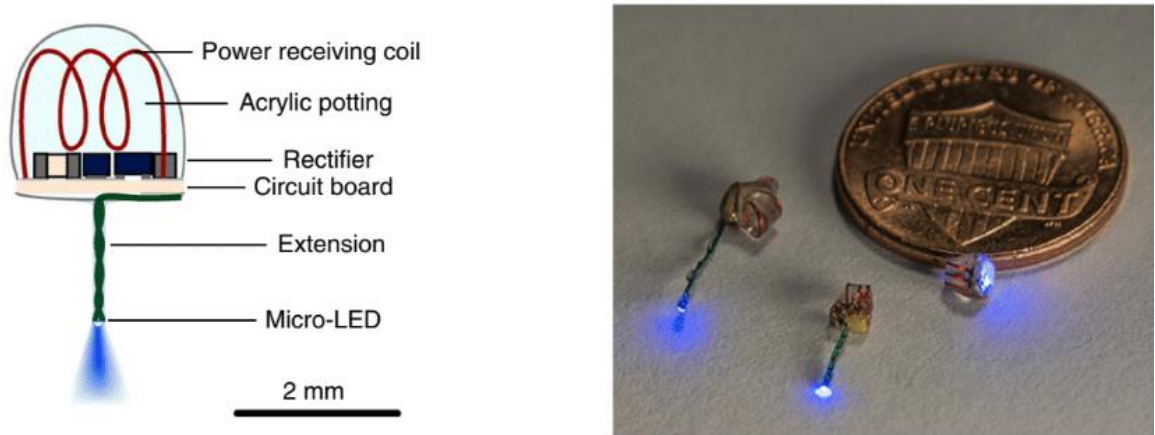
Figure 1.8: A mm-sized hand-made wirelessly-powered optical stimulator [15]**.**

In [16], authors presented two different configurations for optical stimulation of surface brain tissue (Figure 1.9- left) and deep brain stimulation (Figure 1.9- right). Both of these designs use off-the-shelf discrete components for electrical recording, optical stimulation, and data transmission. They both also utilize a microcontroller to control the

optical stimulation lighting pattern. The device designed for surface brain stimulation uses an addressable array of µLEDs as the light source and a discrete coil to receive inductive power. The amount of harvested power is enough to selectively illuminate one of the LEDs through the LED array. On the contrary, the prototype suitable for deep brain stimulation uses optical fibers to deliver the light to the target tissue. Due to the inefficient coupling between the LED and the optical fiber, this version needs a high power LED (30mW) to deliver enough power to the target tissue. As a result, inductive power is not enough to supply the required power for this design and a miniaturized Lithium polymer battery is used in this version. Same as the previous designs, use of discrete components does not allow scaling the fabrication process for these devices. In order to maintain a stable optical power over a period of time, the LED is operating using a constant current regulator (NSI50010YT1G, On Semiconductor) and a MOSFET switch.
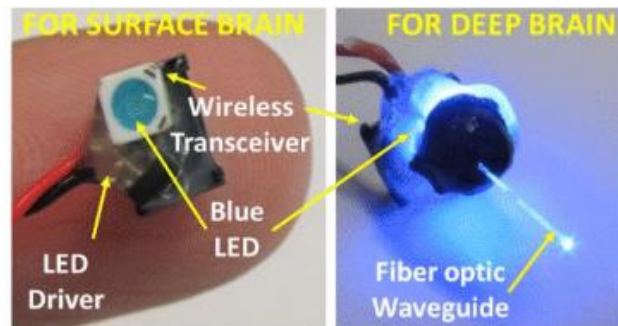
Figure 1.9: (Left) Optogenetic device designed for surface monitoring. (Right) Optogenetic device designed for deep brain optogenetic stimulation (both from [16])**.**

An on-probe electrical recording and optogenetic stimulation is presented in [17] (Figure 1.10 (left)). A custom microfabrication process is used to fabricate the optrode,

which is compatible with both commercial LEDs and built-in LEDs. A standard CMOS IC will be then flip-chip bonded on this passive structure. This design is also capable of controlling output light intensity. However, the LED driver circuit used in this design is only capable of providing current in range of 0-1.1 mA, which is an order of magnitude less the common standard in the optogenetics studies [18]. Moreover, for implanting this device inside the scalp either a battery or inductive coil should be used to deliver the required power to the chip, both resulting in significant increase in the device physical size and/or weight. In this design, in order to minimize the net electric field across the implantable components, an H-bridge configuration is adopted (Figure 1.10 (right)), which allows for a biphasic electric field.
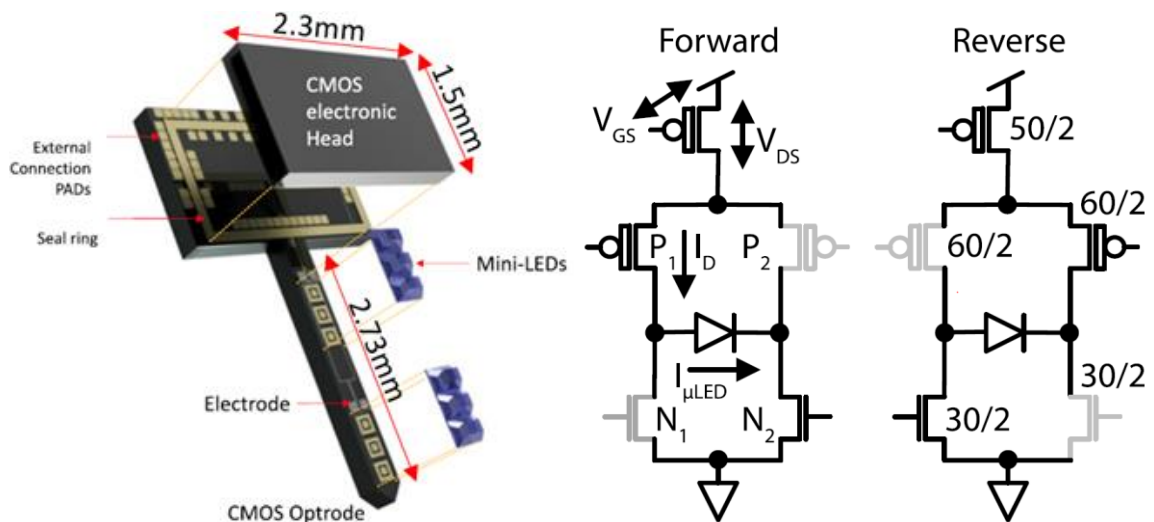
Figure 1.10: Left: Conceptual view of the optrode manufactured for electrical recording and optogenetics stimulation presented in [17]**. Right: The H-bridge LED-driver circuit in forward and revere biasing configurations.**

Recently, a free-floating wirelessly-powered 16-channels implantable optical stimulation system on a chip (SoC) was presented in [19] (Figure 1.11). This design uses an array of µLEDs as the light source, but due to the limited amount of the inductively-delivered power, only one LED can be selected and turned on at any time.

In this work the LED driver circuitry is designed under the presumption that a decaying exponential waveform is the most efficient way of optical stimulation due to previous experimental results for electrical stimulation with different patterns [20]. However, this assumption has not been proved for optical stimulation and due to the fundamentally different procedure underlying optical and electrical stimulation, this may be a false conclusion.

As a result of this speculation, the stimulation pulse pattern in this design is always a decaying exponential waveform mainly due to the fact that instead of a current-mode driver, the LEDs are turned on by discharging the resonance capacitors of the inductive power link into the LED. Removal of driving circuits results in saving area and power consumption at the cost of losing control on the stimulation pulse waveform magnitude and shape (e.g. pulse, ramp, etc). The other problem of a decaying exponential waveform is that once we get away from the initial peak, and for a large part of each pulse, the current magnitude supplied to the LED is not enough to generate sufficient irradiance power required for any optogenetic stimulation. This means that some portion of the current consumed is not used for tissue stimulation, hence, wasted.

An important issue that is taken into account in this design is the fact that the radiation angle of µLEDs is almost 180 degrees; therefore, a large portion of the generated light is shone on non-target cells. In other words, enhancing the light directivity will avoid wasting a large portion of the wirelessly-received energy. To do this, an array of custom-designed micro-lenses were separately fabricated (details in [21]) and bonded to the main system, which includes the microchip as well as the discrete components required for the inductive power reception.
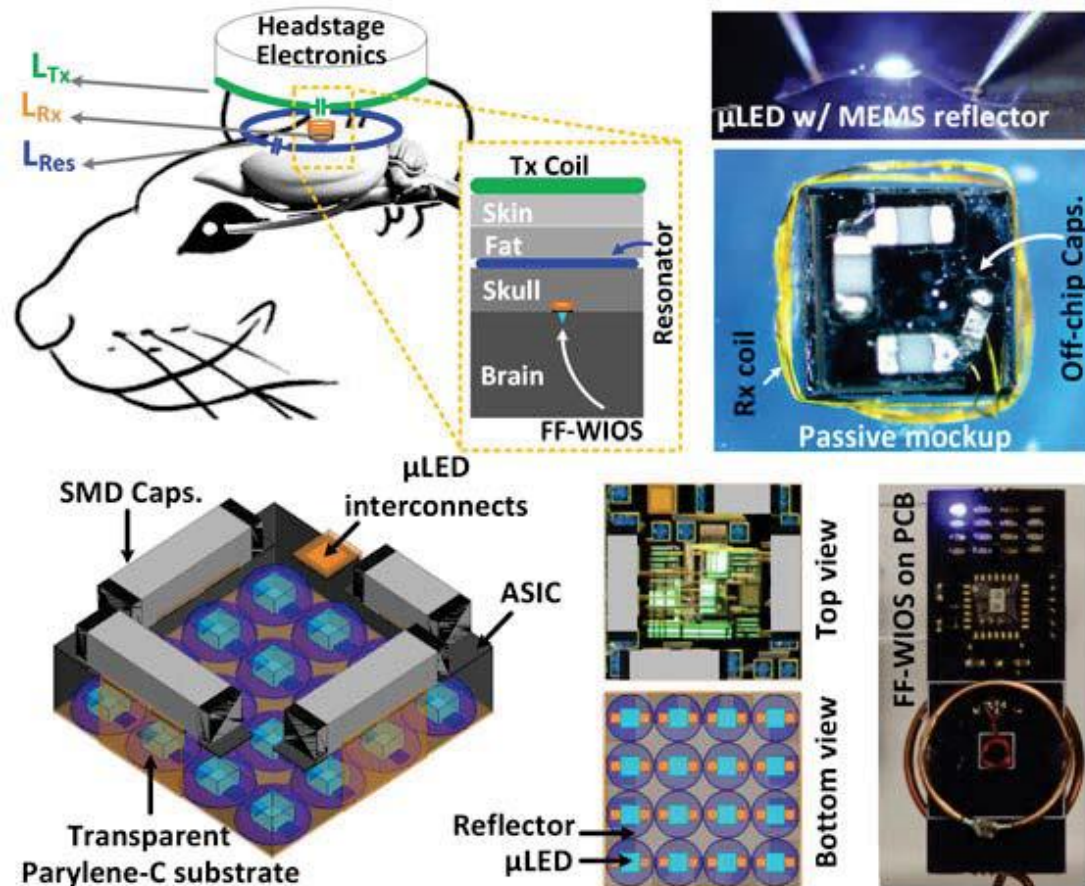
Figure 1.11: A conceptual view of the FF-WIOS system wirelessly powered with a 4×4 LED array on a 3.3×1.2cm^2 PCB presented in [19]**.**

14

1.6 Conclusion

Reviewing the state of the art shows that the direction in the design and development of tools for optogenetic studies is toward the realization of a fully-implantable device. To evaluate the efficacy of the experiment, such a device is preferred to be capable of neural signal recording. It should also be able to precisely control the stimulation pulse waveform parameters (e.g., magnitude, width, etc.) required for different types of experiments and implantation scenarios [22].

In terms of power supply, earlier reported prototypes relied on battery as their source of energy [16], [12] to make the system fully tetherless. However, recent works are moving toward providing the power through a wireless link (e.g., magnetic induction) to allow for long-term animal experiments and long-term human implantations [16], [19]. While the wireless powering link is certainly beneficial, some important considerations should be taken into account:

- The size constraints of a brain-implantable device as well as the SAR (specific absorption rate) limits set by the FDA (Food and Drug Administration) [23] enforce a very tight limit on the maximum power transferred to the device continuously. This is an order of magnitude smaller than the power required to turn the most efficient LEDs on for an effective optogenetic stimulation. Therefore, in addition to the wireless powering need, there is a need for a temporary power storage element (e.g., a super capacitor or a rechargeable battery) on the device to accumulate the received power and release it in a controlled manner during the stimulation.

- The temporary storage element is also limited by the physical size constraints of the device. This sets an upper limit for the number of LEDs that can be active at the same time. Otherwise, increasing the number of LEDs available on the system without being able to activate them simultaneously comes at a very small benefit.

Based on the above, in addition to all the features that should be included in the optogenetic device, perhaps the most important goal in development of these devices is improving power efficiency. This could be done through fabrication of a novel LED with better power conversion efficiency (i.e., optical power / electrical power), or through better circuit and system design, such as deigning a LED driving circuits with adaptive voltage compliance. Another approach to achieve a better power efficiency is through light directivity enhancement techniques, such as implementing a dome-shape micro-lens on top of the LED to converge the light. Converging the light not only can increase the power efficiency by focusing all the output light to the target point, but also can increase the spatial resolution of the optical stimulation by narrowing the ray trajectory of the LED output light.

1.7 Objective and Organization

The main objective of this work is to design, fabrication, and experimental validation of a power-efficient wirelessly-powered implantable microsystem for simultaneous optogenetic stimulation and electrical recording.

Figure 1.12 depicts the envisaged approach for implanting this free-floating micro-systems on the brain cortex, where each device that is comprised of a 3×4 mm^2 SoC with

two $270{\times}220$ um^2 µLEDs, each coupled with an optical micro-lens, assembled on top of it (full system description in Chapter 2). The fabricated chip also include two differential recording channel and the conductive pads on the chip play the role of the electrodes.
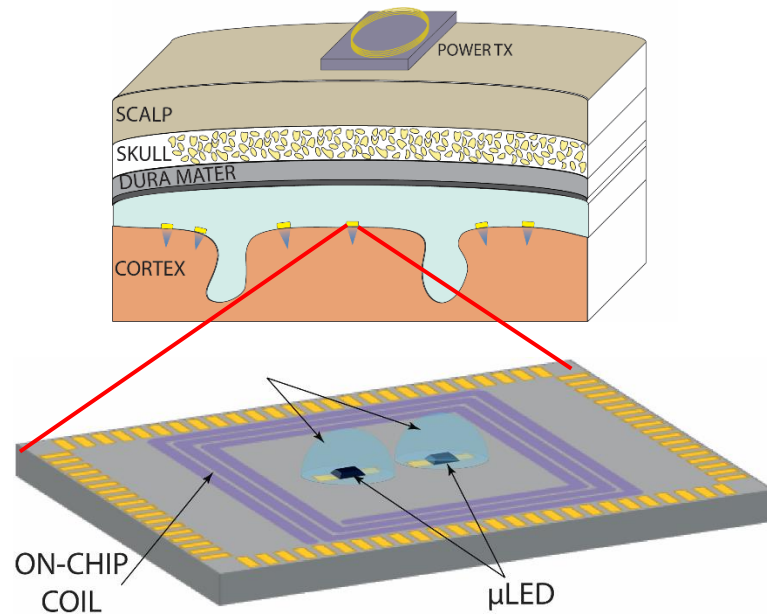
Figure 1.12: Proposed implantable device for simultaneous optical stimulation and electrical recording with on-chip coil, equipped with micro-lenses on top of the µLEDs.

The SoC hosts electronic circuits for both optical stimulation and electrical recording (i.e., amplification and digitization). The stimulation circuitry allows for full control of magnitude and timing of pulses for each channel individually. It also integrates a $2{\times}2$ mm^2 inductive coil as well as rectifiers and regulators for inductive power reception.

A novel current driver circuit (described in Chapter 3) is employed to minimize the required voltage supply for driving the µLEDs, therefore maximizing the power efficiency. To further improve the energy efficiency of the device, an optical dome-shape micro-lens

is designed, optimized, and fabricated to be placed on top of each LED in order to enhance its light directivity. The entire process of design, optimization, and fabrication of the lenses through additive manufacturing is presented in Chapter 4.

Chapter 2

System-Level Design

Considerations and Optimization

This chapter presents the system-level design considerations and components optimization of the targeted optogenetic implantable medical device. First, the system-level design requirements are described and our approach to address each challenge is explained. Then different design techniques used for optimizing the device performance in terms of light directivity and energy efficiency, together with supporting COMSOL Multiphysics simulation results are presented.

2.1 Optical stimulation requirements

The first step to design an optogenetic stimulation device is to define the required specifications such as light source type, number of channels, stimulation light pattern, physical size, power budget, etc.

2.1.1 Light Source and light delivery choices for optical stimulation

The most common choices for light generation in an optical stimulation device are LEDs (Light Emitting Diode) and LDs (Laser Diode), and the main delivery methods are using an optical fiber, optrode, or implanting the μLED in close proximity of the target tissue.

Using optical fiber results in a tethered connection, prevents the full implantation of the system and increases the possibility of an infection due to the length of the fiber. However, placing the light source outside the body would relax the design constraints in terms of power consumption, which directly affects temperature increase, compared to a fully implanted solution. For this type of light delivery both LEDs and LDs are viable choices, but, since LDs generate a coherent light (i.e., no abrupt phase changes), it is a better choice for coupling light into the optical fiber as it yields a better coupling efficiency (i.e., smaller loss of power at the interface). Using an LED as a light source for an optical fiber connection results a coupling efficiency as low as 2 percent [5]. The only reason that some optical-fiber-based systems still use the LEDs is their lower cost compared to the LDs and the fact that since the light source is outside the body we may be able to increase the generated power as much as needed to deliver the targeted optical power to the brain tissue.

The next choice is using optrodes or opto-probes. These are micro-fabricated semiconductor structures that are small enough to be fully implantable. The light source in this method is usually LEDs located at the tip of the optrode. These LEDs can be a built-in component of the optrode or commercial LEDs placed on a standard, typically silicon-

based, structure. Various examples of such designs are presented in [17], [24], [25]. Since all the LEDs on the optrodes are controlled by the same back-end circuitry, stimulating different cells in a relatively large area of the brain (e.g., a few cm^2) results in optrodes with physical sizes that are not acceptable for implantation due to safety issues. In addition, a big issue with this method is the requirement of a custom microfabrication process that is different from the standard CMOS process used for implementation of stimulation and possible neural recording circuits. Therefore, the final device might require complex packaging schemes that make its production in large quantities financially impractical/infeasible.

The third method is using mm-scale free-floating devices that host LEDs and are designed to be implanted intracranially and deliver the light directly to the target cells. These self-contained devices integrate the LEDs on the same substrate that the driving circuits are implemented on and include necessary components for wireless and battery-less operation. Similar to the optrode method, adjacency of the light-generating component (LEDs) and the brain cells sets strict power dissipation constrains to avoid tissue damage. However, the distributed paradigm used in the implantation of these free-floating implants (unlike the centralized paradigm used for optrodes where all the circuits were integrated on a single chip) makes these constraints more feasible to achieve, especially as the number of required LEDs increases.

Based on the above discussion, and toward the goal of a many-channel optogenetic stimulation system, we opted for a free-floating SoC that uses commercial high-efficiency µLEDs as the light source.

Following a comprehensive review of commercially-available µLEDs, and comparing them in terms of their physical size, wall-plug efficiency, threshold voltage, etc., CREE TR 2227 was selected. It is available in two wavelengths of 450nm and 527nm. This LED has a footprint of 220×270 µm^2, which takes close to 1.5% of the 2x2 mm2 overall planned area of the free-floating SoC. Figure 2.1 illustrates the I-V characterization of this LED for its two wavelengths. As shown, for both cases, the LED current reaches to the commonly-accepted maximum required for optogenetic stimulation (i.e., 10mA) with a driving voltage of less than 3V. As it will be more discussed in Chapter 3, this is of critical importance for implementation using a standard (non-high-voltage) CMOS technology, and consequently, avoiding substantial energy loss.
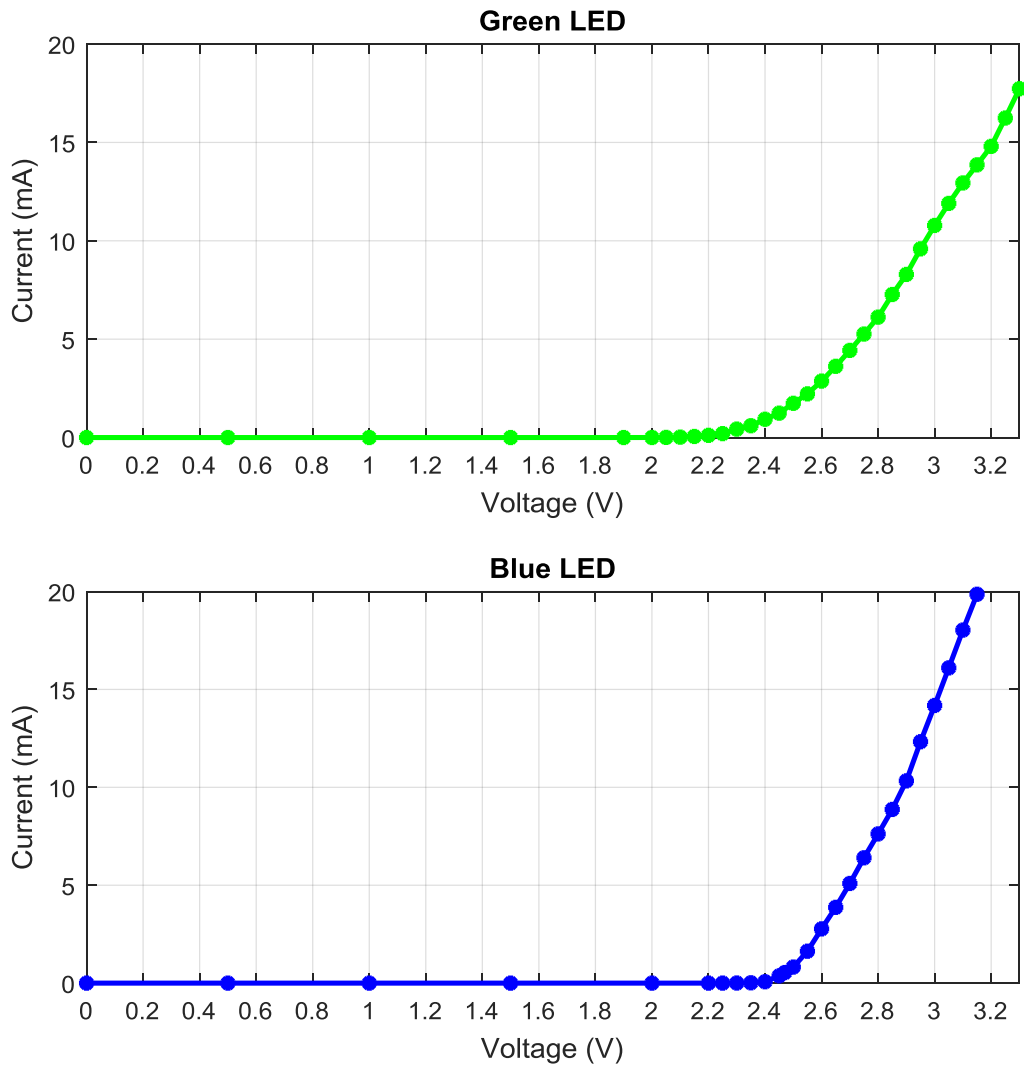
Figure 2.1: Measurement results for I-V characterization of the target LED (Cree TR2227)

2.1.2 Number of channels

Given the typically-high driving currents for optogenetic stimulator LEDs (1 to 10mA, drawn from a supply voltage of >3.3V), simultaneous stimulation using an array of LEDs is not quite practical yet. Additionally, given the small size of the entire device (appx 3×4 mm^2), achieving high spatial resolution does not seem feasible as the light radiated from

different LEDs will shine to significantly overlapping area, unless an extremely high light directivity could be achieved. Considering the above, we decided to only integrate two LEDs on our device. Of course, if the above-mentioned constraints are addressed in the future (e.g., low-threshold highly-directive LEDs) the presented system has no obstacles to host a μLED array. One channel (i.e., the μLED and its driving circuitry) is assigned to the blue light and the other one is for emitting green/yellow light. With this channel assignment, we can trigger various neural behavior for different experiments. The blue LED has excitatory effect on the ChR2 opsin family the green/yellow LED has inhibitory effect on the NpHR opsin family.

One example of medical application in this regard is seizure suppression in epilepsy patients. As presented in Fig 2.4, one of the main known reasons for epilepsy seizure is the positive feedback generated between Cortiothalamic (CT) neurons and Thalamocortical (TC) Neurons [26]. One method to break the link of this positive feedback is directly inhibiting the TC neurons and the other method is exciting the thalamic reticular nucleus (nRT) neurons, which are proved to have inhibitory effects on the TC neurons. This simple example evidently shows the superiority of optogenetic stimulation over electrical stimulation since the direct inhibitory effect is only applicable in optogenetic stimulation. Moreover, [27] suggests direct inhibition is more effective than indirect inhibition to successfully suppress epilepsy seizures.
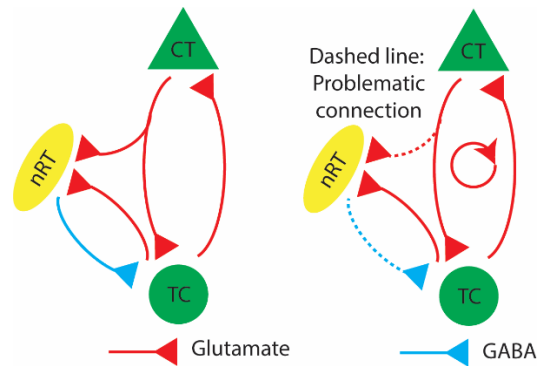
Figure 2.2: One example of CT-TC-nRT network during normal state (left) and seizure (left) (Picture modified from [27])

These two LED colors are also required for activating and deactivating the step function opsins and therefore are useful to modulate complicated neuronal behaviours. [28] suggests possibility of ultimate control of neurons with spatial resolution of sub-diffraction area like a single dendritic spine using these two colors to modulate SFO integrated neurons.

2.1.3 Stimulation patterns

Optogenetic stimulation is a novel area of research and there are many research questions awaiting investigation with the suitable stimulation devices. For instance, from electrophysiology point of view, it is crucial to explore specific response of various types of opsins to optogenetic stimulation with different light intensities and lighting patterns such as ramp vs pulse-light stimulation [22]. With this in mind, we tried to design an optogenetic stimulation device capable of generating different lighting patterns such as

ramp and pulse with controllable lighting frequency and duty cycle as well as possibility of controlling the output light intensity.

2.2 Directivity enhancement

Directivity enhancement of the LED radiation is the other goal of this project. The radiation pattern of the regular LEDs is around 180° wide. Figure 2.3 illustrate the radiation pattern of the CREE TR 2227 LED [picture used is taken from the LED datasheet].
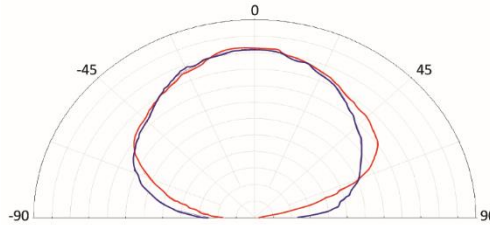
Figure 2.3: Radiation pattern for Cree TR 2227 [Cree TR 2227 datasheet].

This wide illumination pattern has two obvious drawbacks. First issue is that, this pattern of radiation limits the spatial resolution of the optical stimulator. This means that even if sufficient power is delivered to the mm-scale implantable device, turning n µLEDs in an array will have a very similar effect to turning one of those µLEDs with n times more current, simply because the area illuminated by all the LEDs in the array are, more or less, the same. In this work, we fabricate and integrate a dome-shaped micro-lens, which directs the output light of the LED, hence, yielding a higher spatial resolution.

The second issue originates from the fact that the optical power intensity of the LED decreases by getting further from the center of the radiation pattern. Due to the fact

that the opsins require a minimum light intensity to show any reaction, some portion of the output optical power is wasted, since it does not have enough energy to stimulate the opsins. Our solution of using a micro-lens encompassing the LED solves this problem by directing all the output light to one target point. As presented in Figure 2.4, using a micro-lens will fundamentally increase the efficiency and reduce the power consumption of the optical stimulation design by not just reducing light dissipation but using all the LED output optical power to increase light intensity at the target.
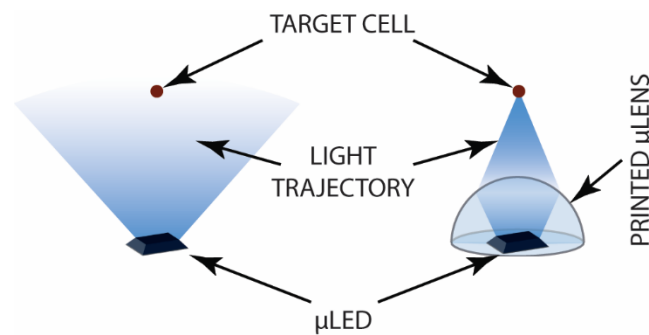
Figure 2.4: Light directivity and spatial resolution with and without the micro-lens.

Since the targeted focus of optical stimulation might vary from a single point to an area of certain shape (e.g., a circle or a ring), it is ideal to be able to fabricate custom micro-lenses of various shapes. Toward this goal, we proposed to fabricate our micro-lens using an inkjet printer. Inkjet printing is a versatile technique for fabricating custom designed micro-lenses for various applications [29]. Figure 2.5 depicts some of reported configurations for custom designed micro-lenses using inkjet printing. Beside the possibility of fabrication of custom-designed micro-lenses for specific applications, inkjet

printing allows for quick and low-cost fabrication of such lenses in large quantities, making the commercialization of the presented device financially feasible.
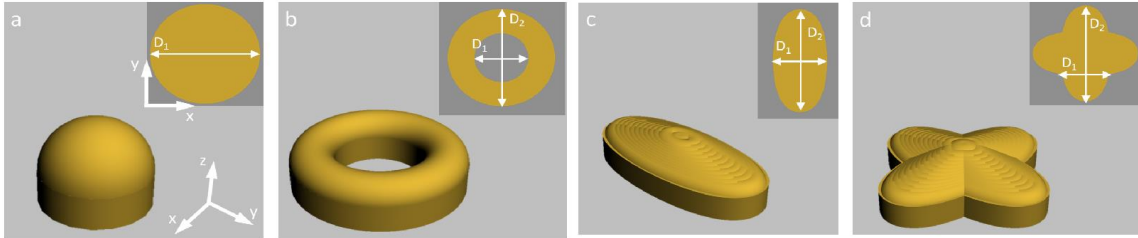
Figure 2.5: Representation of custom-designed micro-lenses for different applications [29]**.**

As mentioned in chapter 1, there has been another report of using micro-lens in an optical stimulator device. The light-directing structure presented in [21] consists of a frontside micro-lens and a backside reflector to gather all the output light of the LED. However, this micro-lens require custom microfabrication process, which makes it unsuitable as a scalable solution. Additionally, unlike the inkjet printing, the presented process in [21] is specific to a dome-shaped lens and cannot be used for other shapes without substantial changes. However, in first step of this project we decided to implement a dome-shape micro-lens since it can converge the LED light very efficiently, while having a straightforward fabrication process.

2.3 Micro-lens optimization

Design and optimization of the micro-lens is done using COMSOL Multiphysics v5.4. Among the various shapes possible, a dome-shaped micro-lens was decided to be designed and optimized for this device. Through the course of optimization, different structural

parameters of the dome were determined. Micro-lens optimization in this work emphasises on focusing the light on a specific target tissue, which is located in a perpendicular known arbitrary distance from the implant.

Figure 2.6 outlines the micro-lens+µLED spherical-planar geometry. The optimization process mainly depends on the placement of the implant with respect to the target tissue. This model is developed based on the assumption of locating the implant inside the cerebrospinal fluid (CSF) with an optical refractive index n_2. Additionally, the target point is at a known distance inside the brain tissue with a refractive index n_3 and the target area is assumed to be $10\times10\mu m^2$, which is in order of a single neuron size [30]. This model can be simply adjusted for different scenarios, for example, placing the implant in the same medium as the target tissue or defining different layers between the implant and target tissue or for a different target area.
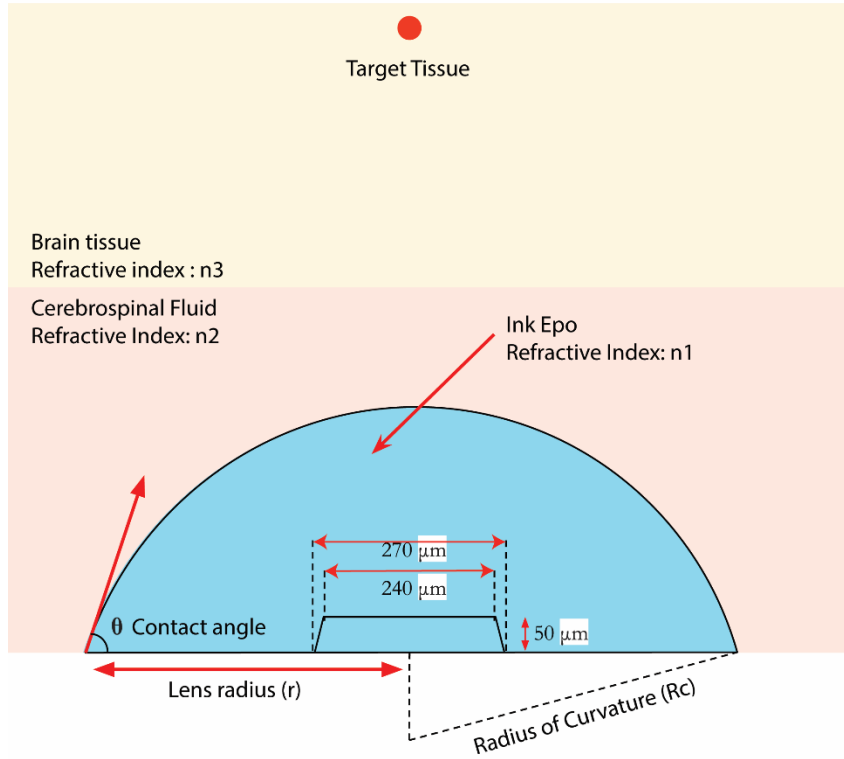
Figure 2.6: Spherical-planar geometry of micro-lens + μLED.

The main parameters that defines the micro-lens geometry are lens radius, radius of curvature, and the focal length. However, in our model, the contact angle of the lens is a process-related parameter and is calculated to be 60°. Therefore, given the radius of curvature (R_c) and the contact angle (θ) of the lens, the lens radius is given by Equation (2.1).

$$r = R_C \sin \theta \tag{2.1}$$

The radius of curvature itself is a function of effective focal length based on Equation (2.2).

$$\frac{1}{f_{eff}} = \frac{(n_1 - n_2)}{n_2} \times \frac{1}{R_C} \qquad \text{(2.2)}$$

where n_1 is the refractive index of the lens materials (InkEpo in this case) and n_2 is the refractive index of surrounding medium.

Figure 2.7 presents our model of implant location inside the CSF and the target tissue. Based on our developed model in order to count for the interface between the CSF and the brain tissue, we have to calculate the effective focal length (f_{eff}) based on the target distance. (Equation (2.3))

$$f_{eff} = d_{implant} + \frac{n_2}{n_3}\left(d_{target} - d_{implant}\right) \qquad \text{(2.3)}$$
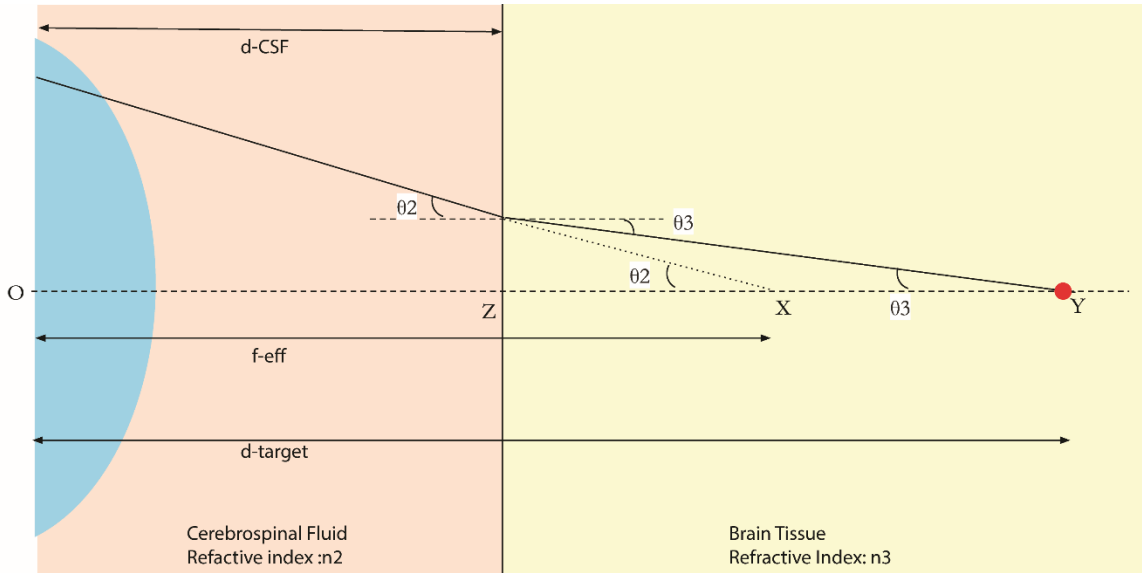
Figure 2.7: Implant loaction in respect to the target tissue.

The optimization simulation has been done for different LED wavelengths to optimize the micro-lenses for each of the LEDs. Different refractive indexes for different

31

wavelengths result in slight difference in final configuration for optimal lenses for different LEDs.

Figure 2.8 illustrates the isometric view of the developed COMSOL model for the micro-lens and μLED combination. The LED shape has been presicely modeled based on the information in the datasheet. The placement of the LED-lens combination in the CSF with respect to the target point located inside the brain tissue is presented in Figure 2.9.
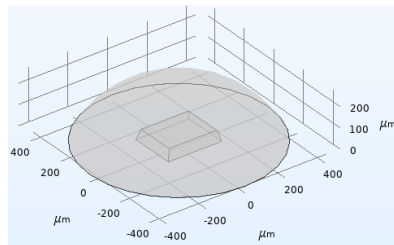
Figure 2.8: Isometric view of the micro-lens and μLED.
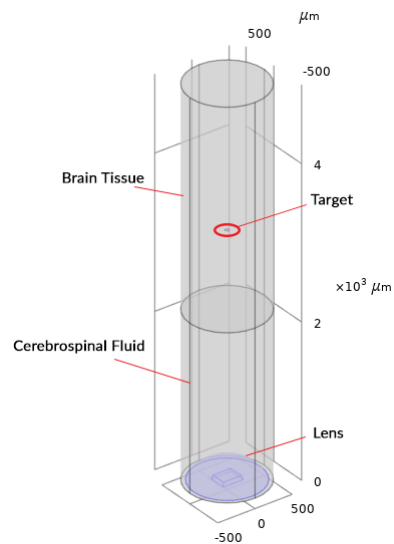
Figure 2.9: The developed COMSOL model for the μLED and micro-lens inside the CSF and the target inside the brain tissue.

32

COMSOL simulation of the ray trajectory of the LED inside the model cylinder including the CSF and the brain tissue display the effect of the micro-lens in converging the output light. The optimization is done such that the target tissue is placed at the focal point of the micro-lens. Figure 2.10 illustrates the ray trajectory of the LED light with and without the presence of the micro-lens.
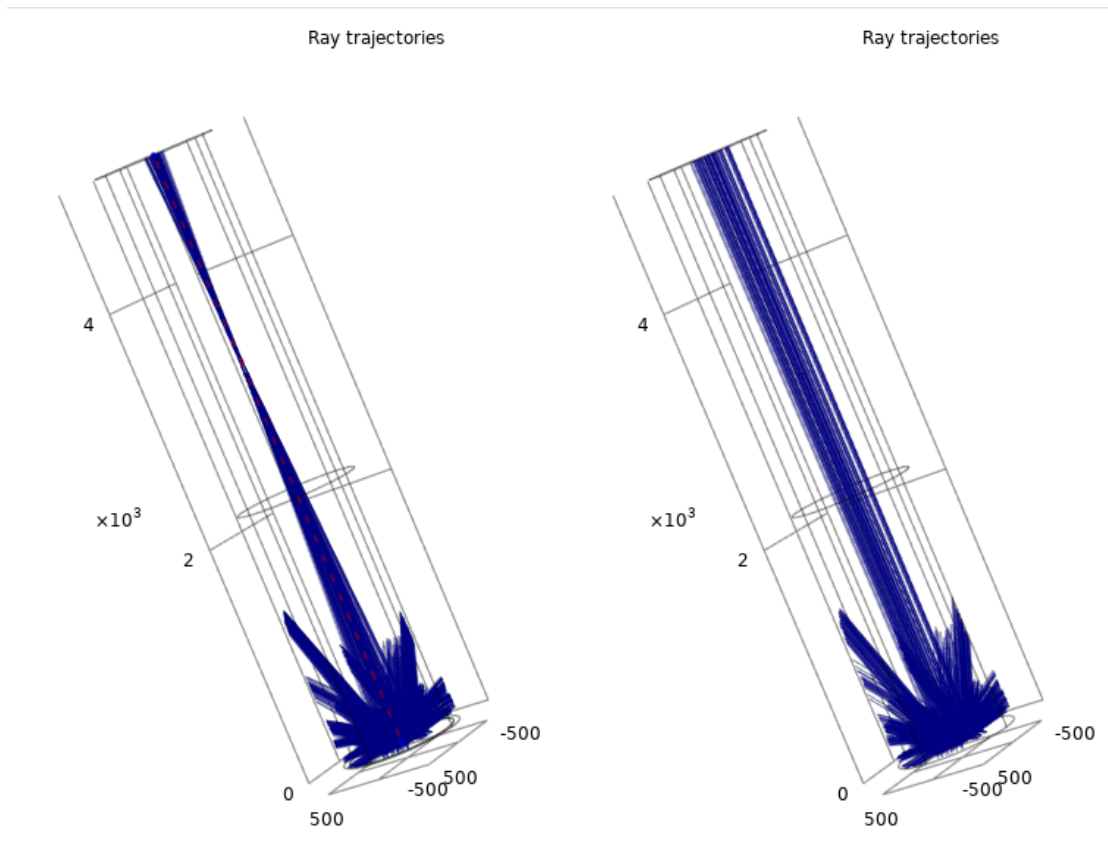
Figure 2.10: LED output ray trajectory with (left) and without (right) the lens.

As presented in Figure 2.11, COMSOL simulation is done for temperature distribution to ensure the operation is done within the safely limits. Our simulation reveals that although converging the light will increase the heat dissipation at the target point,

existence of the micro-lens will block part of the heat and therefore, result in less temperature increase inside the tissue. This simulation shows the micro-lens results in focusing the heat in close proximity of the LED, while for further points than the target, the temperature increase is actually less that the model without the micro-lens.
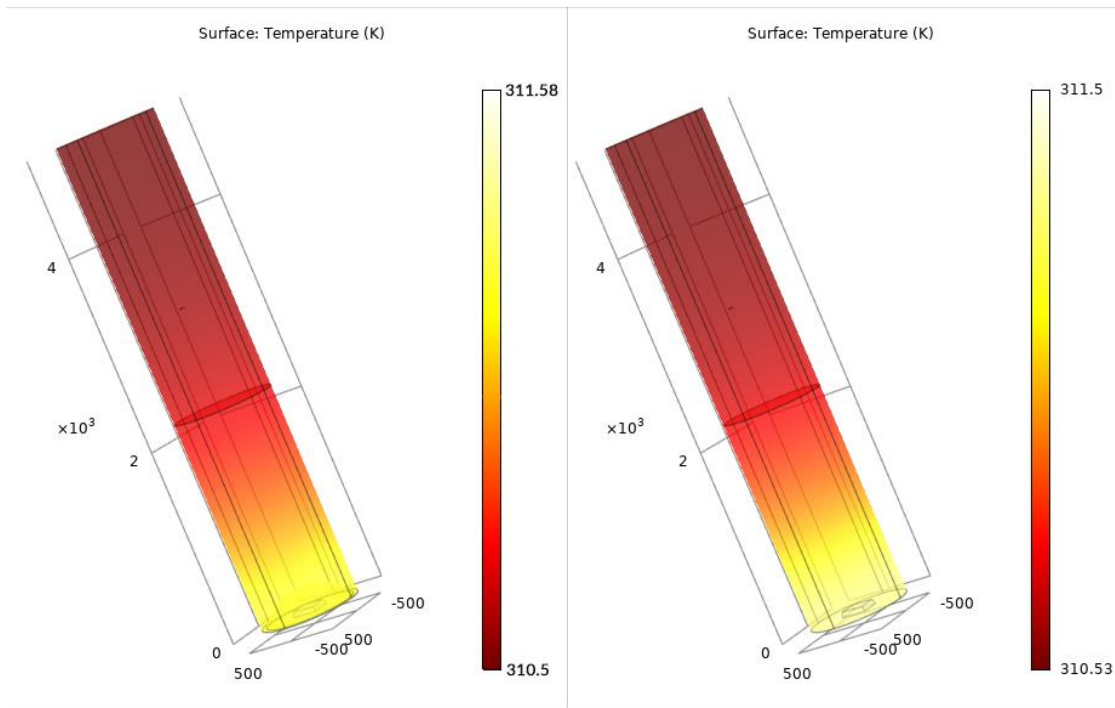
Figure 2.11: Temperature simulation with (left) and without (right) the lens.

Table 2.1 reports the optical power and maximum temperature inside the CSF and brain tissue for blue and green LED with and without presence of the micro-lens. Clearly, it can be seen that introducing a lens in all cases increases the received optical power (and hence irradiance) at the target. The temperature distribution simulation also confirms that placement of the µLED will not break the boundaries of safe amount of temperature increase around the implant.

Table 2.1: Optical power and maximum temperature inside the CSF and brain tissue.

Blue LED	LED type	Power (W)	Max. Temp in BT (K)	Max. Temp in CSF (K)
With Lens	Blue LED	8.53E-05	310.73	311.32
Without Lens	Blue LED	2.79E-06	310.78	311.67
With Lens	Green LED	9.62E-05	310.70	311.20
Without Lens	Green LED	3.16E-06	310.74	311.51

Chapter 3

Fully Implantable Optogenetic Stimulator and Electrophysiological Recording

This chapter presents transistor-level circuit design and characterization of the fully-implantable self-contained dual-channel neural recording and power-efficient optical stimulation SoC. Figure 3.1 shows the top-level block diagram of the presented SoC. As shown, two stimulation and two recording channels are integrated on the chip. The stimulation channels are controlled digitally and can generate currents in the range of 1 to 10mA with a resolution of 3 bits. Each recording channel includes a two-stage capacitively-coupled amplifier followed by an 8-bit successive approximation register (SAR) analog to digital converter (ADC). The recording channels are included to study the brain response to various optical stimulation parameters such as current magnitude, waveform type and shape, frequency of stimulation, etc. The SoC also includes an on-chip inductive coil

connected to rectifiers and regulators that generate supply and bias voltages required for its operation.
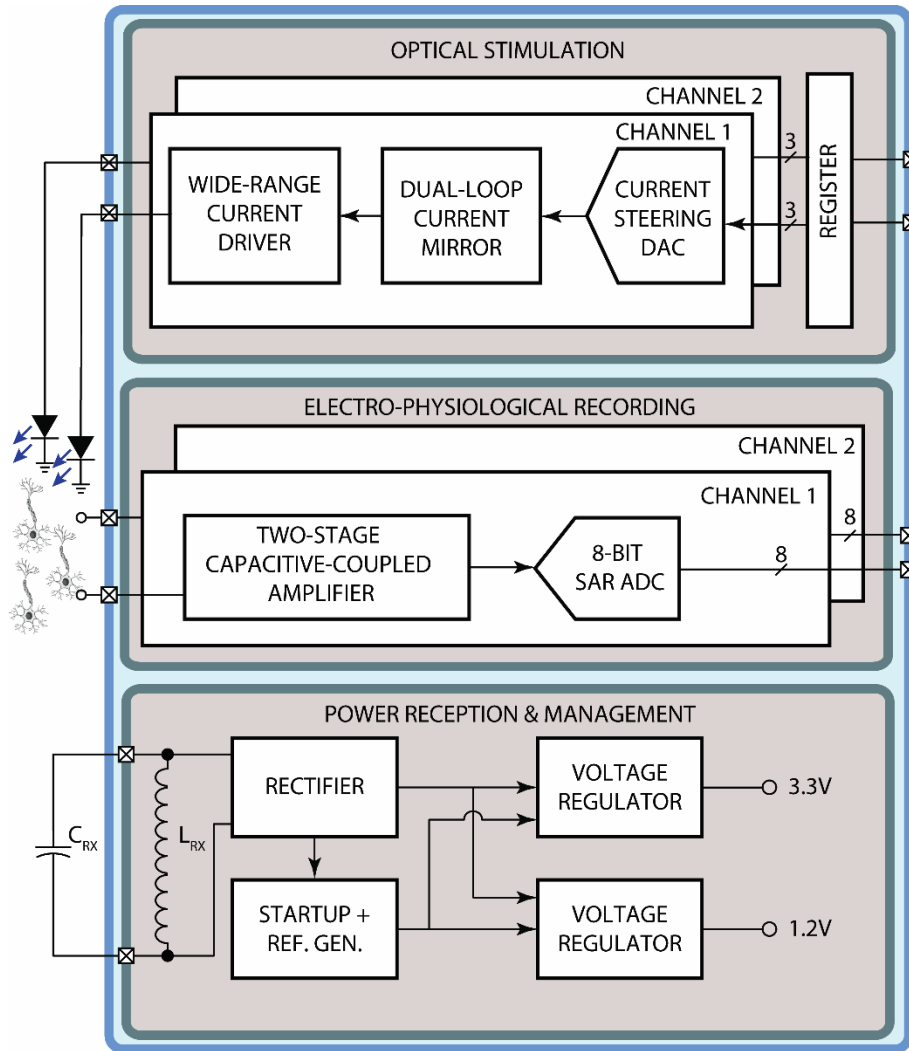
Figure 3.1: Top-level block diagram of the presented SoC.

In this chapter, we will describe the detailed circuit implementation of each of the above-mentioned blocks, with a particular attention to the stimulator circuit and the novel design we have proposed for its current driver. Prior to the circuit-level design descriptions,

a brief, yet important discussion on the major bottlenecks in terms of energy efficiency of an optogenetic stimulator is provided to emphasize on the critical role of a power-efficient driver circuit for the stimulation channels. The chapter ends with characterization results of he presented SoC and comparison to the state of the art.

3.1 Energy efficiency in optogenetic stimulators

Power efficiency is one of the main constraints in designing any implantable SoC. For optogenetics stimulation, it is required to deliver a wide range of optical power to the target tissue to investigate the behaviour of a specific opsin under different circumstances [22]. For the majority of commercial or custom μLEDs used in the literature, an electrical current up to 10 mA by the LED driver is sufficient to implement various optical stimulation scenarios [18]. On the other hand, a minimum magnitude of 1mA is typically required to generate the sufficient irradiance to trigger a neural response. With such a stimulation current range drawn from a minimum 3.3V supply voltage, and considering that the power consumption of all the other blocks included in the recording or stimulation channels of the system shown in Figure 3.1 is in order of micro-Watts, the LED-driver will dominate the system power consumption. Therefore, any attempt in decreasing the power consumption of the LED driver will directly affect the power efficiency of the whole system.

Power efficiency consideration in an implantable optical stimulator can be divided into four different categories.

1) *Power efficiency of the inductive link:* which means what percentage of the transmitted power is actually received, rectified and regulated and is available to the SoC blocks for their operation. While we do have an inductive powering module implemented on this SoC, we will not discuss the details of its implementation and operation in this thesis as it is done by another team member.

2) *Power efficiency of the optical driver circuitry:* which means what percentage of the overall power used to generate the required current for the LED is consumed in the LED, and what percentage was dissipated in the driver circuit. In this work, a power efficient LED-driver circuit is designed, which is explained in details in Section 3.2.

3) *Wall-plug efficiency (radiant efficiency) of the LED:* Wall-plug efficiency (WPE) is the LED efficiency in converting the electrical power to optical power. In this work, we used a Cree TR2227 LED as the light source, which is claimed to have the best WPE between the LEDs with similar size.

4) *Light delivery method efficiency:* which means what percentage of the generated optical power is indeed delivered to the targeted point(s) on the brain cell. Locating the LED in proximity of the target tissue for direct light delivery and placing a micro-lens encompassing the µLED to focus the output light to the target tissue, are our solutions to have a power efficient light delivery method.

3.2 Optical stimulation circuit design

Figure 3.2 shows a simplified diagram of an LED driver circuit. There are many variations of this circuit reported in the literature, but they all include a current driving circuit that has at least one component (e.g., a transistor) in series with the LED to control its current. Ideally, the channel should be designed in a way that all branches except for the LED branch draw µW-level currents from the supply, making them negligible to the mA-level LED current. As a result, power consumption of the optical stimulation is roughly equal to $VDD_{LED} \times I_{LED}$. Therefore, to minimize the power consumption we either have to minimize I_{LED} or VDD_{LED}. The required current through the LED (I_{LED}) is determined by the neurological application and what light intensity it requires. In addition, the voltage across the LED (V_{LED}) for any specific current is determined based on the LED I-V characteristics. This leaves the voltage across the LED driver ($V_{LED\text{-}Driver}$) as the parameter that should be minimized to realize an efficient implementation. The power dissipated in this component (i.e., $V_{LED\text{-}Driver} \times I_{LED}$) could be quite significant, given the high typical values of I_{LED}.
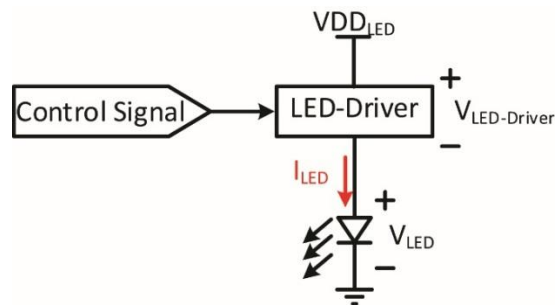
Figure 3.2: Simplified circuit diagram of the digitally-controlled LED driver.

40

For the LED used in this design (Cree TR2227), a current range of 1 to 10 mA translates into a voltage range 2.5 to 3V across the LED. As for the available supply voltage, we had to first look into different options for CMOS integrated circuit fabrication technology nodes. For the described SoC, we needed a technology that provides both high frequency transistors for wireless power telemetry circuits as well as a relatively-high (e.g. >5) number of metal layers that allow for integration of a large system on a chip. On the other hand, going to more advanced nodes (e.g., beyond 90nm) had the problems of (a) high leakage currents, a big problem for ultra-low-power implantable devices, (b) significantly higher cost, and (c) most importantly limited supply voltage of 1.2V that could not drive the LEDs. considering all of the above, CMOS 180nm and 130nm technology nodes seemed to be optimal as they allow a high level of integration (8 metal layers), integration of RF circuits (3 thick metal layers), driving the μLED (max VDD of 3.3V if thick oxide transistors are used) and relatively low leakage currents.

Reviewing several optogenetic stimulation systems reported in the literature that use commercial or custom-designed μLEDs, the driving circuit requires a voltage headroom of bigger than 300mV, making the minimum required supply voltage higher than 3.3V [12], [16], [19], [31]. In these designs, generating the required voltage for the LED driver circuitry and LED is done by either using a charge pump circuit (e.g., in [31]) or using a higher supply VDD (e.g., in [12]). Using charge pumps to generate a supply voltage higher than the nominal maximum voltage of the CMOS technology comes with the risk of junction breakdown and permanent damage to the chip, which is also a safety issue for

a brain implantable device. On the other hand, use of a high-voltage (HV) technology means the use of transistors with significantly higher threshold voltage, hence, an undesired significant increase in the required supply voltage that directly increases the power consumption.

Figure 3.3 presents a simple LED driver, which consists of a current DAC (digital to analog converter) and a simple current mirror. The main problem with this design is that for Transistors M_1 and M_2 to operate as a current mirror with a reasonable precision and linearity, they should be operating in the saturation mode so that the current is solely controlled by their common V_{GS}. However, the required voltage across the LED for large currents (Approximately 3V) leaves a voltage headroom of around 300mV for the thick-oxide M_1's V_{DS}, which is not enough to bias it in the saturation region. It should be noted that although 300mV might be enough to keep the device in the saturation region when it drives a small current, for a large current, the significantly-high overdrive voltage of the MOSFET (e.g. 1.5V for 10mA) will force it to the triode region. Being in the triode region means the failure of the current driving circuit as it cannot provide a current magnitude that is proportional to the digital control command that it receives.
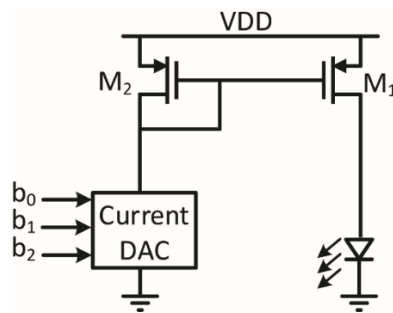
Figure 3.3: Conventional LED driver circuit.

The circuit in Figure 3.4 proposed in [13] provides a solution that allows for precise current mirroring even in the triode region, however, at the cost of having a LED driver headroom voltage higher than 300mV. This design can provide accurate mirroring conditions for M_1 and M_2 by matching V_{GS} and V_{DS} of these transistors. As a result, the voltage across the LED is equal to VDD-$V_{DS}M_1$-$V_{DS}M_3$. In this design, the minimum possible headroom across the LED-driving elements, which are M_1 and M_3, happens when the M_1 transistor is biased at the edge of saturation and the M_3 transistor is pushed to the triode region. This design is also strongly dependent on bias voltage of M_4 transistor, since it has a direct effect on the drain voltage of M_1 and M_2.
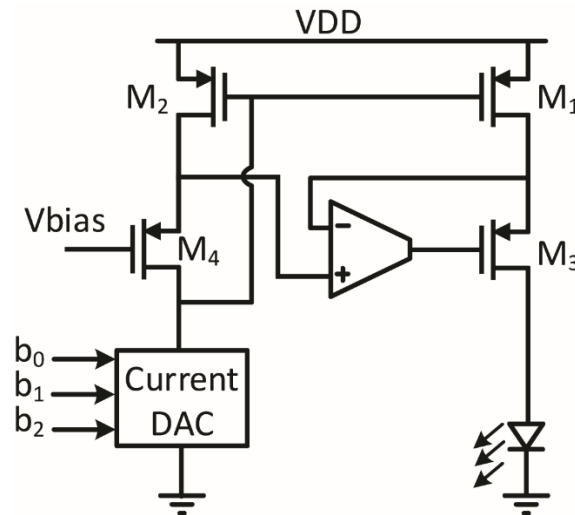
Figure 3.4: current-mode stimulator controllable with a 3-bit current DAC.

A variation of the previous design, which only use one transistor in the LED-driving branch, is presented in Figure 3.5 [32]. This design has one negative feedback loop consisted of the OTA and transistor M_3 and a positive feedback loop consisted of the OTA,

M$_3$, and M$_1$. Therefore, to avoid instability, the positive feedback loop should be designed with a loop gain smaller than unity. [33] defines this loop gain as $\frac{gm1ro1}{gm2ro2+\frac{ro2}{RO}}$, which implies that the stability can be achieved by ensuring similar size for M$_1$ and M$_2$. However, making M$_1$ and M$_2$ of similar size results in them having the same current, which effectively means doubling the channel power consumption, as we need two copies of the LED current now. To avoid this, transistor M$_1$ is always sized to be significantly larger than M$_2$ (e.g., 1000:1). Therefore, this design is prone to instability for our application.
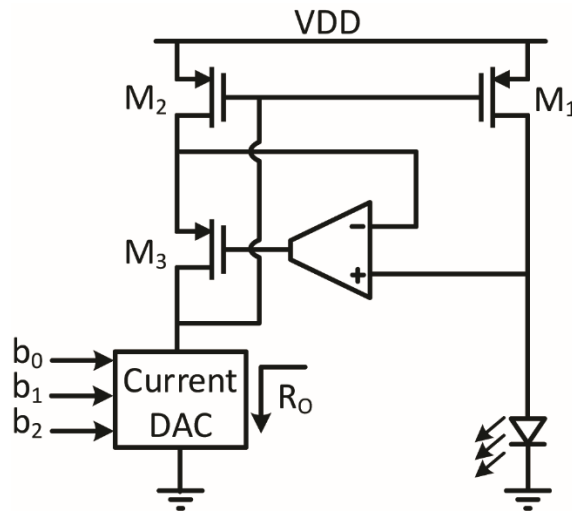
Figure 3.5: Stimulator circuit with one transistor in load branch.

3.3 Proposed optical stimulator design

Figure 3.6 illustrates the stimulator circuit with one transistor in the LED branch with the current DAC connecting to the main circuit using a source to sink topology. In order to break the positive feedback in this design, drain of M$_2$ should be disconnected

44

from gate of M_1 and M_D. On the other hand, for M_3 and M_4 to form a perfect current mirror, they require to have similar V_{DS} as well as similar V_{GS}.
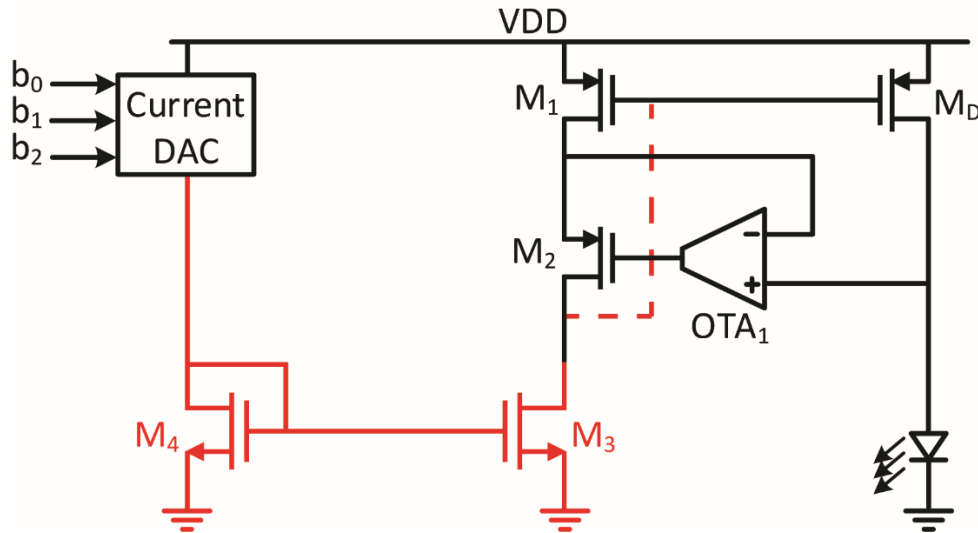
Figure 3.6: Stimulator circuit with one transistor in load branch and a current DAC in source structure.

As presented in Figure 3.7, in our proposed design OTA_2 generates the control signal for gate of M_1 and M_D, while making sure that M_3 and M_4 are forming a perfect current mirror. Table 3.1 lists the sizing information for transistors in the LED-Driver.
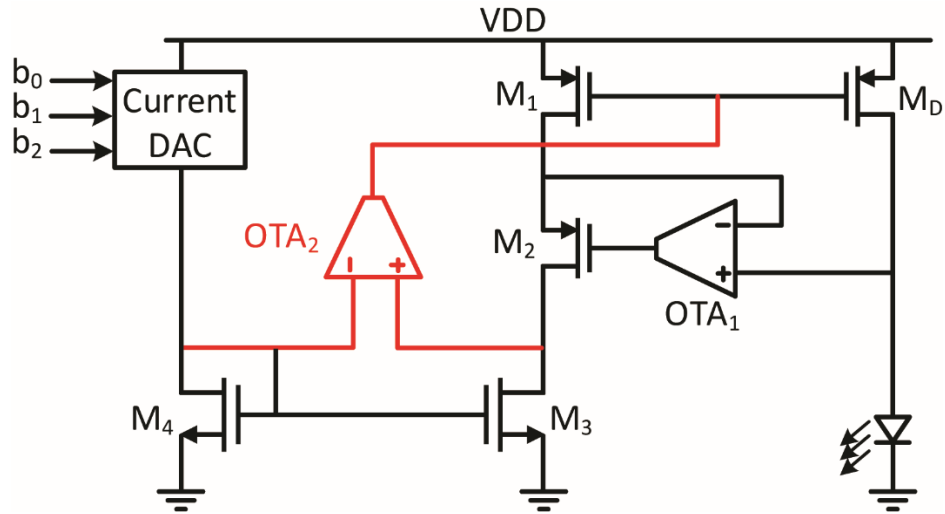
Figure 3.7: Proposed design for a power efficient LED-driver.

Table 3.1: Sizing information for transistors in the LED-Driver circuit.

Transistor	M_D	M_1	M_2	M_3	M_4
W/L	800μ/500n	800n/500n	2μ/500n	700n/350n	700n/350n

Therefore, in this design the reason for having OTA_1 is supplying large currents through the LED leaves very small headroom for the M_D transistor, which will push the transistor to triode mode. Therefore, while transistor M_1 and M_D has similar V_{GS}, it is important for them to have similar V_{DS} to have an accurate mirroring in triode region as well as the saturation region. On the other hand, OTA_2 not only make sure of the mirroring condition between M_3 and M_4, but also it is required to generate the control signal for the gate of transistors M_1 and M_D. This design is also capable of bringing the gate voltage of

M_D and M_1 down to 0 if it is required to generate the required current through the LED which is not possible in any other design.

In this design, there is no constraint on the required voltage across transistor M_D and it can be pushed to the triode region. Figure 3.8 shows that the proposed design has a linear performance for the entire range of interest irrespective of operating region of the LED-driver transistor. This is unlike the conventional design, where the LED current has linear relation to the DAC current, only if the M_D transistor is saturation region.
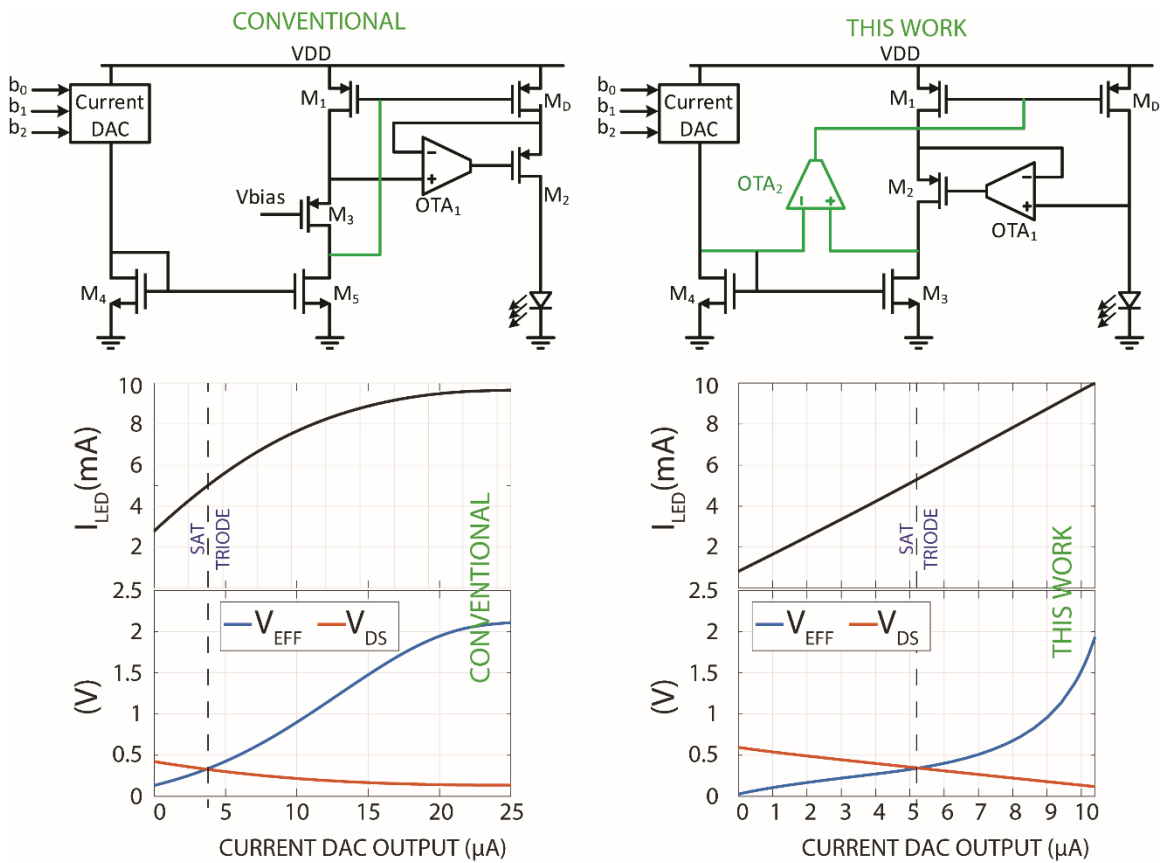
Figure 3.8: Circuit performance comparison with respect to the LED-driver transistor operating range

47

For stability analysis in this design, the stability analysis for the three loops in this design are done using cadence simulation. Figure 3.9 illustrate the three available loops in this design. The stability analysis has all the loops ensure the stability of the design.
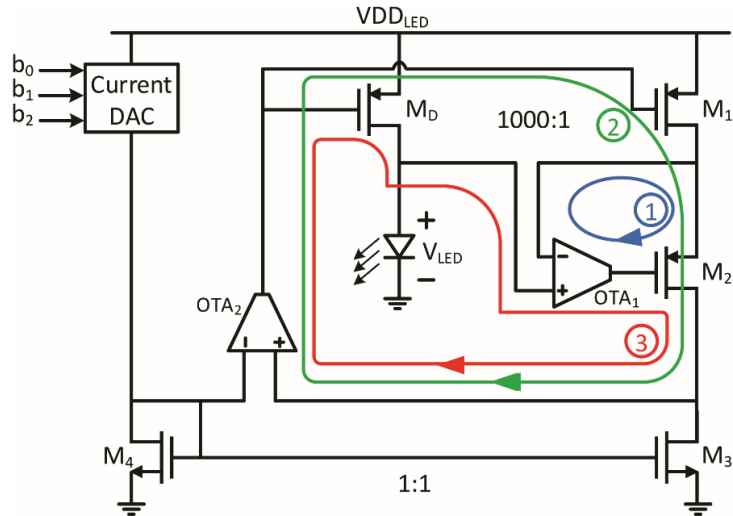
Figure 3.9: Illustration of the loops in the proposed design

Figure 3.10 shows the phase and magnitude of stability analysis for loop 1 by breaking the loop at the output of OTA_1 (gate of M_2). This loop has the phase margin of 74.8° at frequency of 83.55 kHz, which ensures the stability of this loop.

Figure 3.11 shows the phase and magnitude of stability analysis for loop 2 and 3 by breaking the loop at the output of OTA_1 (gate of M_D and M_1). This analysis results in phase margin of 46.6° at frequency of 1.34 MHz, which ensures the stability of these loops.

Figure 3.12 illustrates the simulated LED current for input current in range of 1-10μA, which results in LED current in range of 1-10mA in different corners of process variation and ensures that the process variation would not affect the circuit performance.
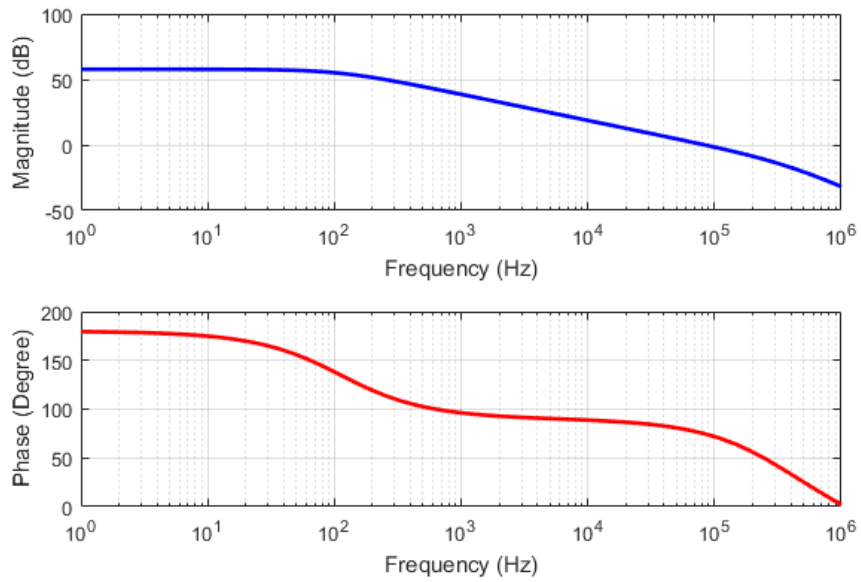
Figure 3.10: Magnitude and phase of stability analysis for loop1.
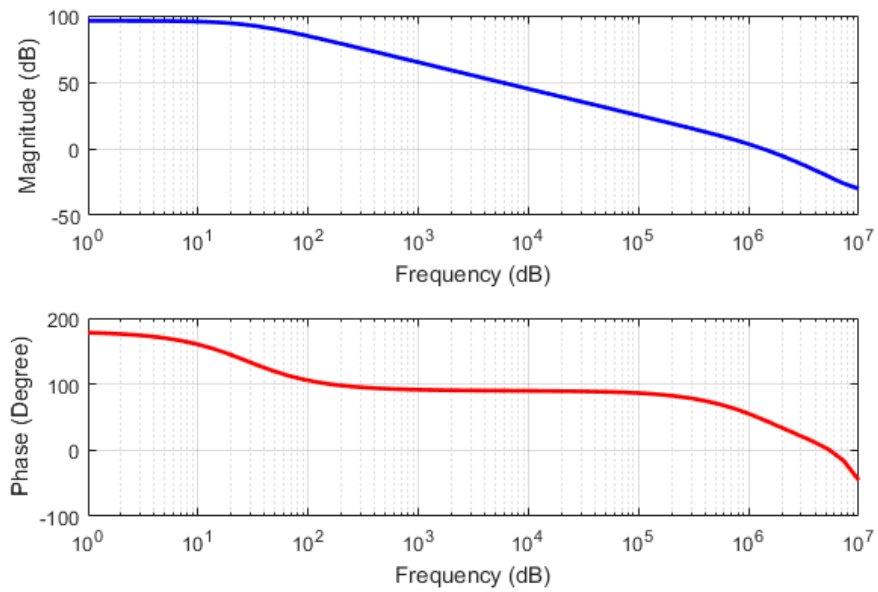
Figure 3.11: Magnitude and phase of stability analysis for loops 2&3.

49
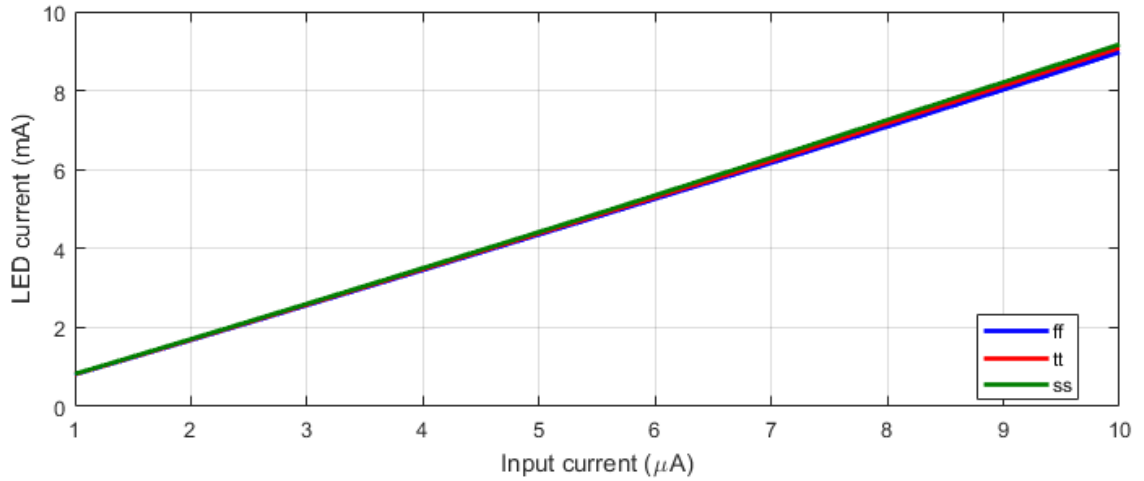
Figure 3.12: Simulated LED current for different corners of process model.

Figure 3.13 shows the schematic of the OTAs that were used in the presented LED driver circuit. As shown a folded cascode architecture is employed. The sizing of the transistors is provided in Table 3.2. Both magnitude and phase Bode diagrams of the OTA shown in Figure 3.13 are shown in Figure 3.15. The high open-loop voltage gain of the OTA ensures that the two input terminals are sufficiently close to each other, and phase margin of 90° ensures stability. Using a compensation capacitor at the output of the OTA lead to phase margin of around 90° to ensure stability. Figure 3.14 presents the bias generation circuit for this OTA and the transistor sizes are provided in Table 3.3.
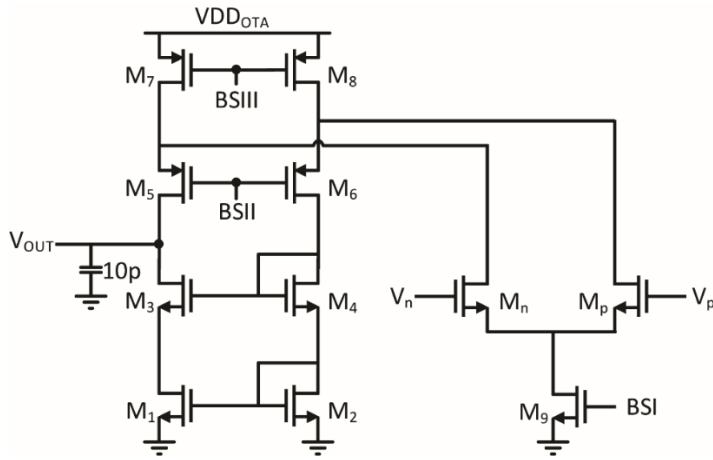
Figure 3.13: Circuit schematic of the high-voltage OTA.
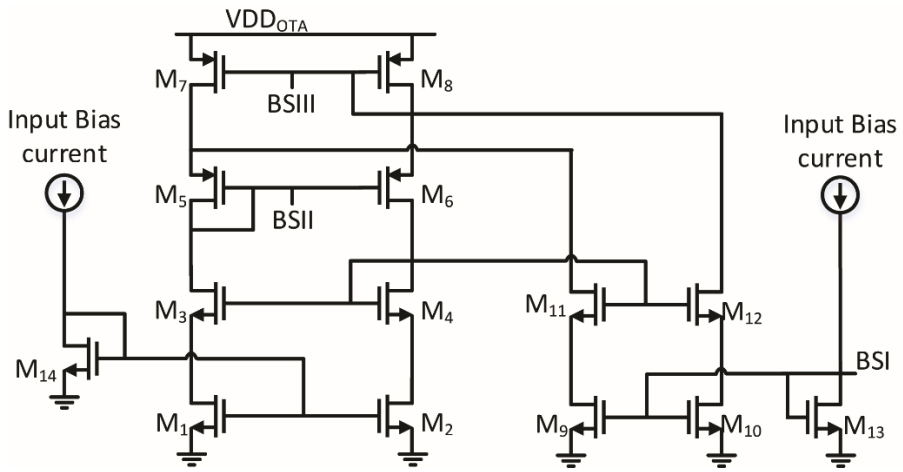
Figure 3.14: Circuit schematic of the bias generator for the high voltage OTA.

Table 3.2: Sizing of the transistors in the OTA used in the optical stimulator.

Transistor	Mp	Mn	M₁	M₂	M₃	M₄	M₅	M₆	M₇	M₈	M₉
W/L	$\dfrac{500n}{500n}$	$\dfrac{500n}{500n}$	$\dfrac{1.2\mu}{500n}$	$\dfrac{1.2\mu}{500n}$	$\dfrac{4\mu}{500n}$	$\dfrac{4\mu}{500n}$	$\dfrac{5\mu}{500n}$	$\dfrac{5\mu}{500n}$	$\dfrac{20\mu}{500n}$	$\dfrac{20\mu}{500n}$	$\dfrac{400n}{350n}$

Table 3.3: Sizing of the transistors in bias generation circuit.

Transistor	M_1	M_2	M_3	M_4	M_5	M_6	M_7
W/L	$\dfrac{1.2\mu}{500n}$	$\dfrac{1.2\mu}{500n}$	$\dfrac{4\mu}{500n}$	$\dfrac{4\mu}{500n}$	$\dfrac{5\mu}{500n}$	$\dfrac{5\mu}{500n}$	$\dfrac{20\mu}{500n}$
Transistor	M_8	M_9	M_{10}	M_{11}	M_{12}	M_{13}	M_{14}
W/L	$\dfrac{20\mu}{500n}$	$\dfrac{2.4\mu}{350n}$	$\dfrac{2.4\mu}{350n}$	$\dfrac{500n}{500n}$	$\dfrac{500n}{500n}$	$\dfrac{400n}{350n}$	$\dfrac{600n}{500n}$
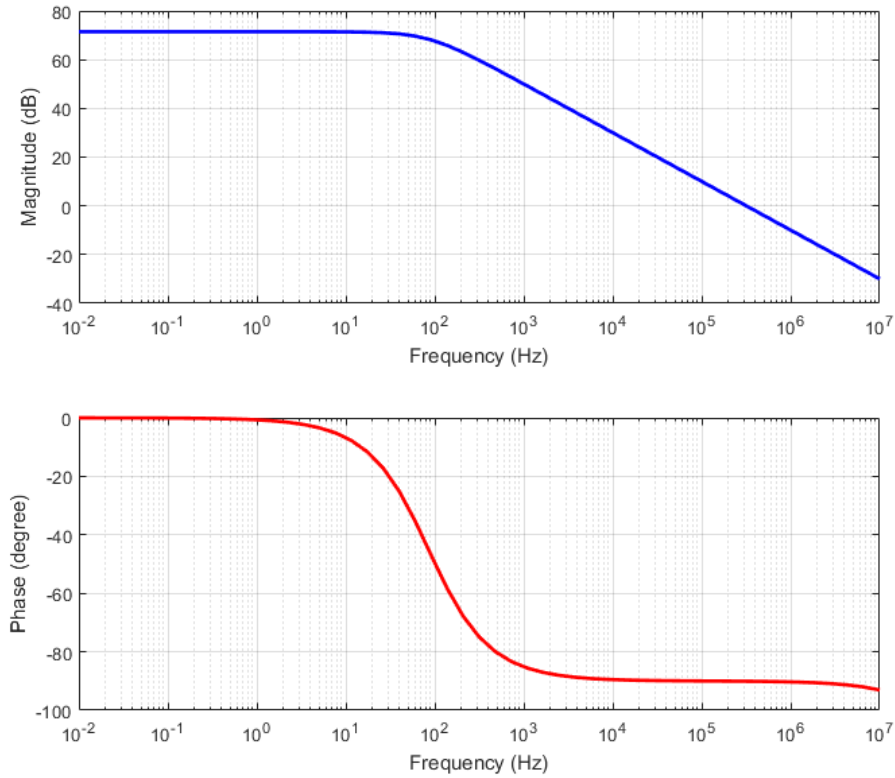
Figure 3.15: Magnitude and phase bode plots of the OTA used in the presented optical stimulator.

The presented stimulation circuit is characterized and the measurement results are presented in the following. In terms of power consumptions, each of the OTAs in this design draw 20µA current from the 3.3 supply voltage and for any desired current through

the LED there are two branches that drawing 0.001 of that current from the supply voltage. To validate the functionality of the 3-bit current steering DAC, Figure 3.16 presents the post layout simulation. Figure 3.17 and Figure 3.18 shows the measurement results for generated LED current for each value of the DAC current for blue and green LEDs respectively.
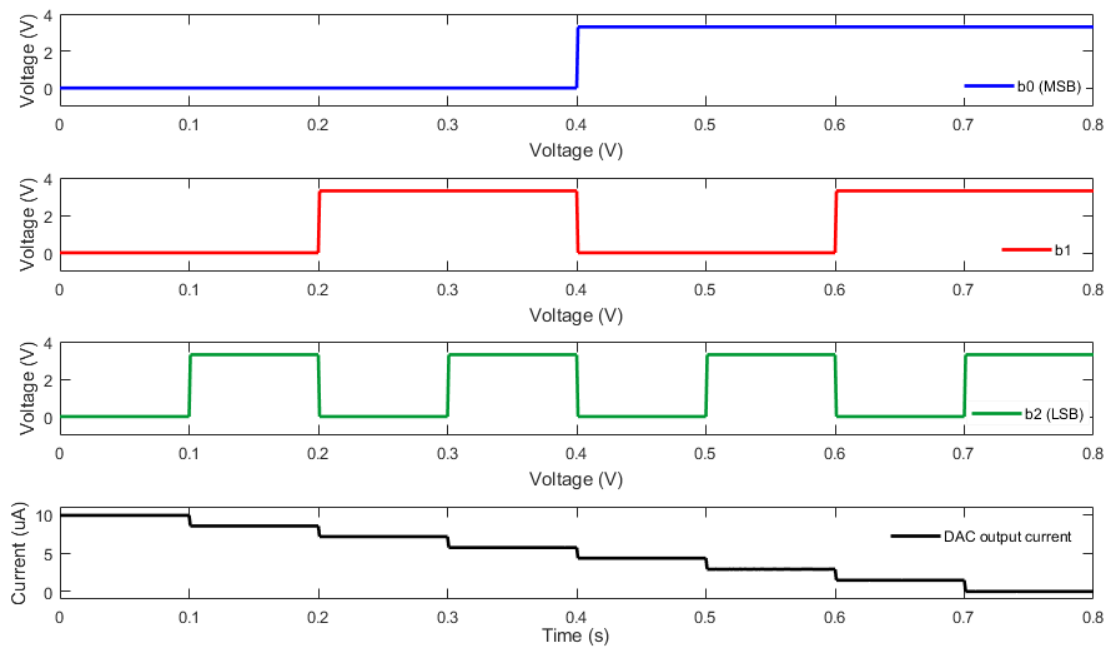
Figure 3.16: Post-layout simulation results showing the functionality of the 3-bit current steering DAC.
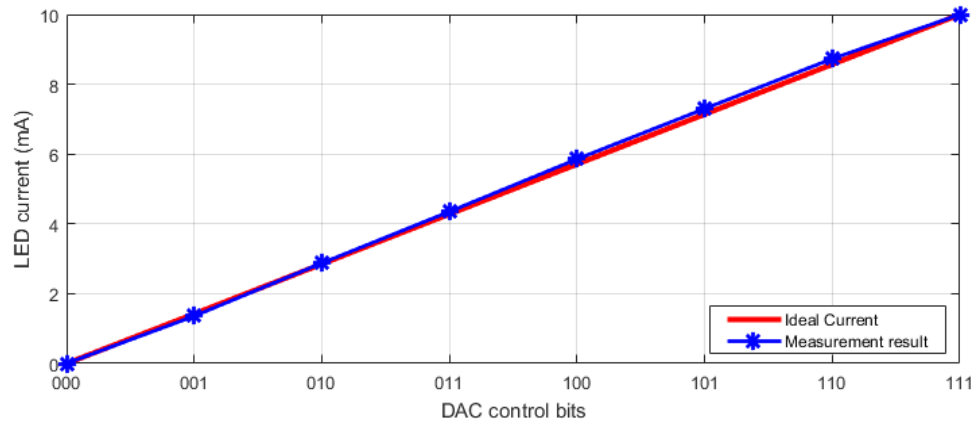
Figure 3.17: Experimentally measured LED current in response to different DAC currents for Blue LED.
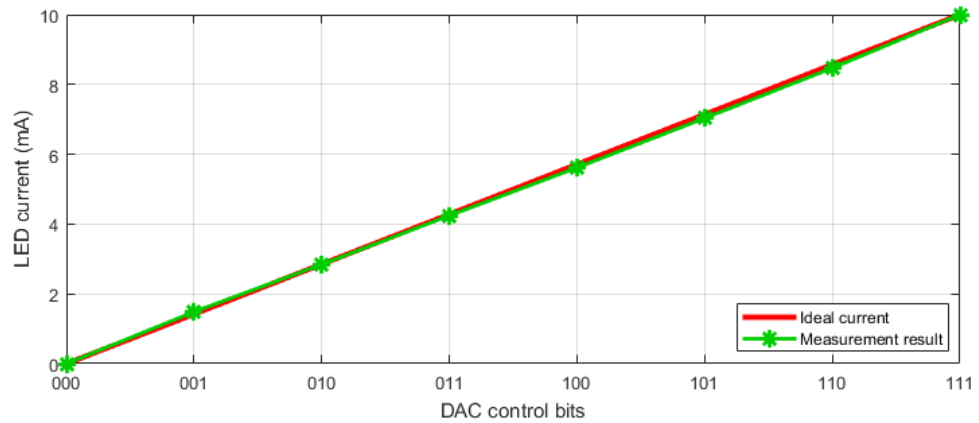
Figure 3.18: Experimentally measured LED current in response to different DAC currents for Green LED.

Figure 3.19 presents the percentage of current mirror error as a function of measured LED current for currents in range of 1 to 10mA for blue and green LEDs.
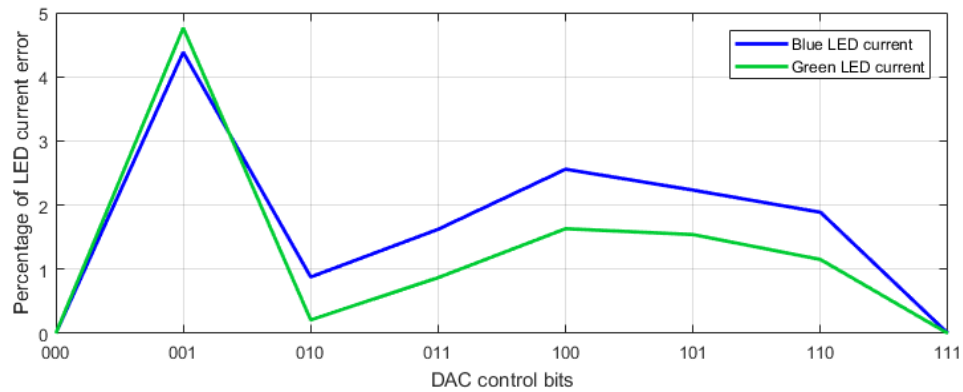
Figure 3.19: Error percentage of the experimentally measured LED current for currents up to 10mA.

Figure 3.20 shows that the current mirror can tolerate as low as 0.2V headroom across the LED-driver element to provide LED current, which has linear ratio with the input DAC current. In this experiment to eliminate the risk of feeding very high currents to the chip, instead of increasing the LED current, we decrease the supply voltage, down to the point that it can generate the maximum current of 10mA with linear ratio with the input DAC current. It should be noted that in our initial simulations, size of M_D transistor has been decided to generate maximum current of 10mA. Our measurements illustrate that the supply voltage can be brought down to 3V, which leaves 0.2V headroom across the LED-driver element for supplying maximum current of 10mA (The measurement is done for the green LED). As presented in Figure 3.21, the minimum required headroom is defined based on size of the LED-driver transistor and can be scaled to allow for smaller required headroom voltages.
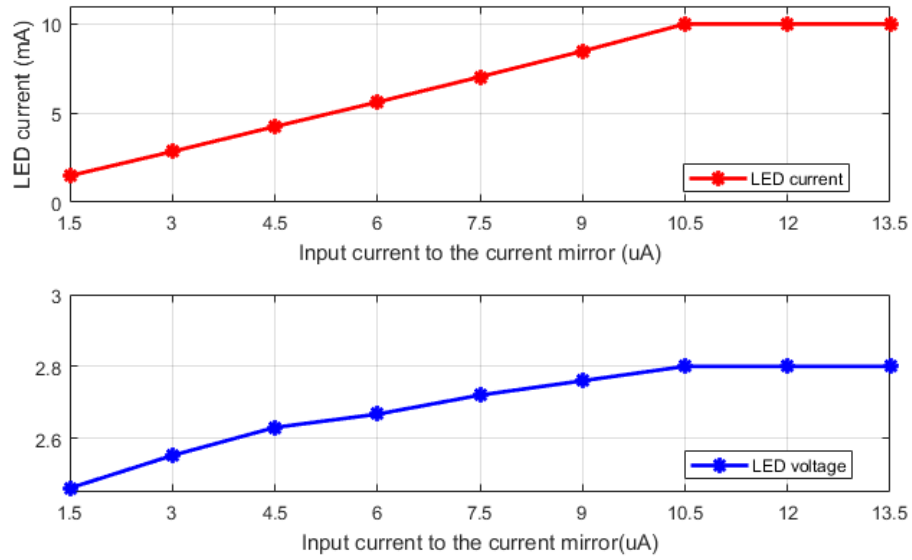
Figure 3.20: Experimental measurement results showing the minimum possible headroom for the LED-driving element.
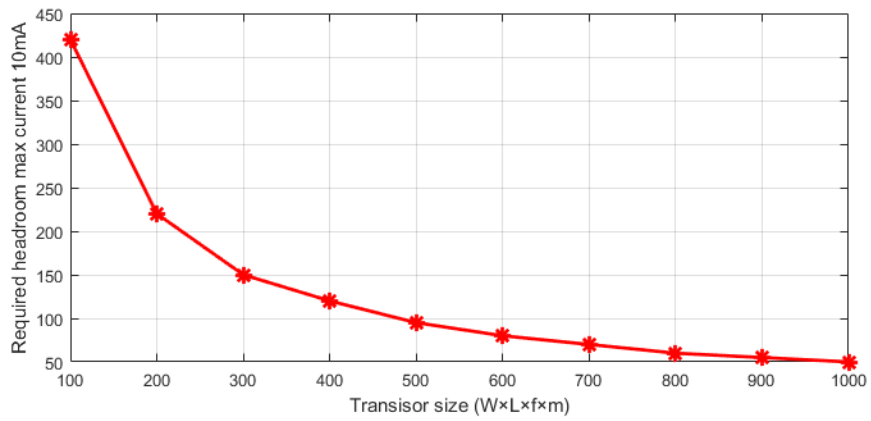
Figure 3.21: Required headroom for max current of 10mA vs size of the driver transistor.

3.4 Electrophysiological recording and digitization

Monitoring the neurological activity of the light-sensitive neurons after optical stimulation is an inseparable part of any optogenetic study and a mandatory requirement if a close-loop control on the optical stimulation pattern and intensity is desired. Therefore, each channel in this system is equipped with an electrical potential recording circuitry to monitor the electrophysiological activities of the neurons. The recording channel used in this work has a conventional two-stage capacitively-coupled architecture inspired by works presented in [34], [35] . Figure 3.22 presents the schematic of this recording channel and Figure 3.23 illustrate the simulated frequency response of the recording channel for different corners of process variation, which confirm that the process variation would not affect the designed gain and bandwidth. The analog output of this recording channel is then digitized using a conventional 8-bit SAR ADC with binary weighted capacitors (c_{unit}=100fF), and measurement results acquire SNDR of 40.15 and ENOB of 6.39 bits for sampling frequency of 8.77kHz and input frequency of 200Hz. Figure 3.28 illustrate the PSD (power spectral density) of the SAR ADC output (number of FFT points =8192). Figure 3.24 presents the schematic of the strong-arm comparator and Table 3.4 reports the sizing of the transistors of the comparator. As presented in Figure 1.12 this device is supposed to be placed on the brain cortex and therefore, the device sizing, passive element selection, and biasing of the amplifier and the ADC are chosen to ensure that it can record local field potential (LFP) signals in the range of 10uV to 1mV, with an integrated input-referred noise smaller than

10uVrms, and a bandwidth of few Hz to 500Hz [36]. All of the above are met while trying

to minimize the power consumption and silicon area usage of the channel.

Figure 3.25 presents the schematic of the OTA in the first stage, which is a fully differential

amplifier. Figure 3.26 presents the second-stage OTA that is a single-ended amplifier.

Table 3.5 and Table 3.6 report the transistor sizing for both of these OTAs. Figure 3.27

shows the measurement results of the recording channel characterization for input referred

noise, gain and bandwidth, which result in gain of 48.5dB over bandwidth of 3Hz to 1kHz

and integrated input referred noise of $9.98\mu V_{RMS}$ over the same frequency band.
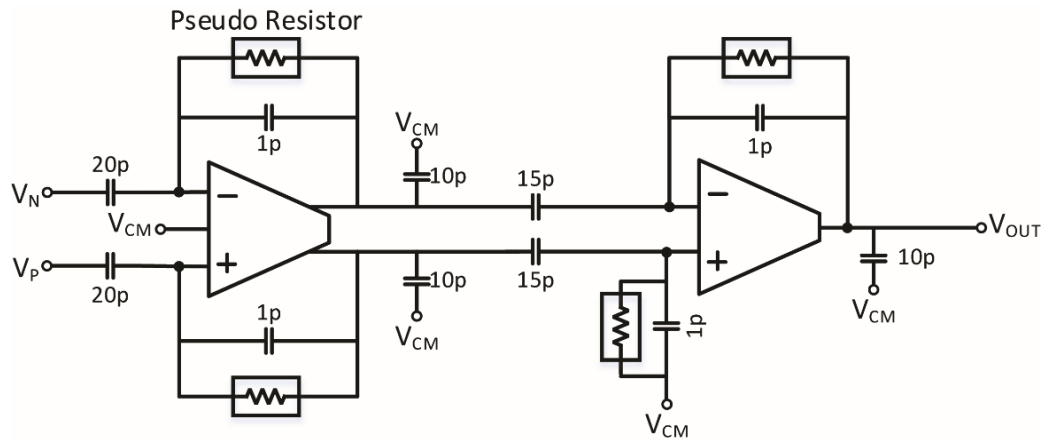
Figure 3.22: Schematic of the recording channel.

58
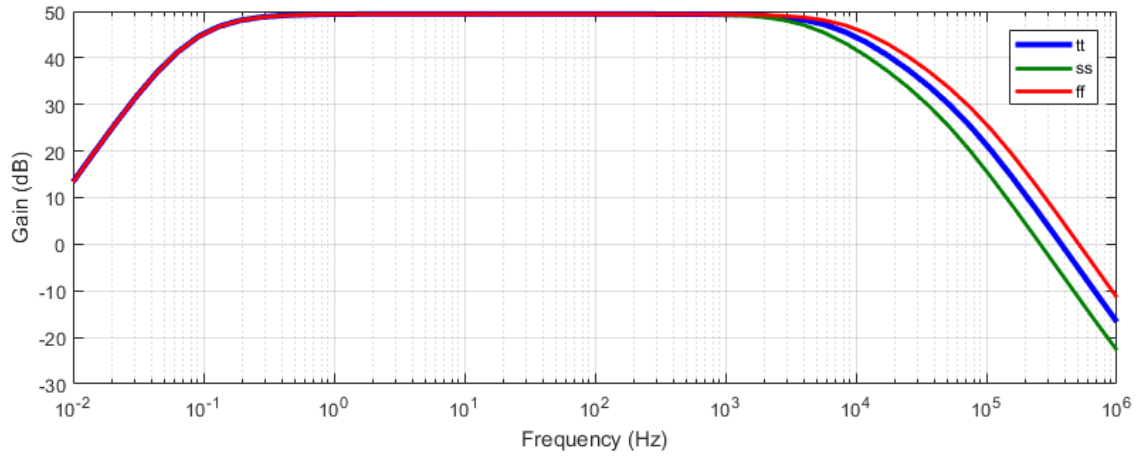
Figure 3.23: Simulated gain of the recording channel for different corners of process model.
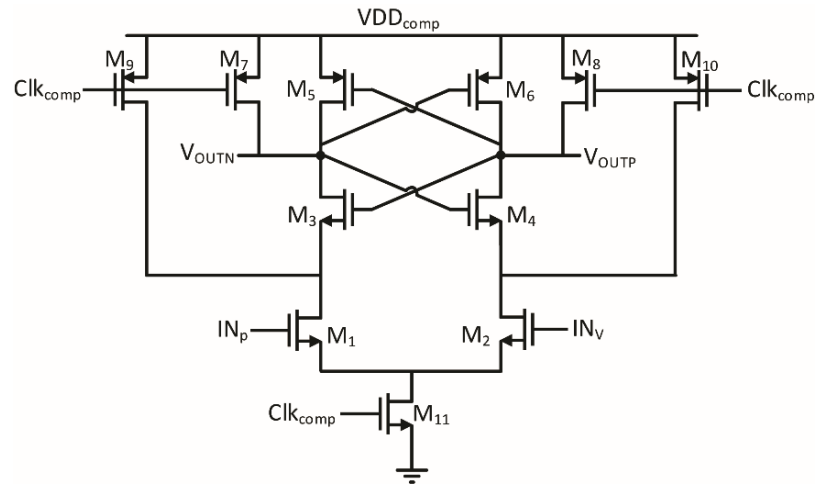
Figure 3.24: Schematic of the strong-arm comparator.

Table 3.4: Sizing of the transistors in the strong-arm comparator.

Transistor	M_1	M_2	M_3	M_4	M_5	M_6	M_7	M_8	M_9	M_{10}	M_{11}
W/L	$\dfrac{250n}{250n}$	$\dfrac{250n}{250n}$	$\dfrac{250n}{250n}$	$\dfrac{250n}{250n}$	$\dfrac{750n}{250n}$	$\dfrac{750n}{250n}$	$\dfrac{1.25\mu}{250n}$	$\dfrac{1.25\mu}{250n}$	$\dfrac{2.5\mu}{250n}$	$\dfrac{2.5\mu}{250n}$	$\dfrac{500n}{250n}$
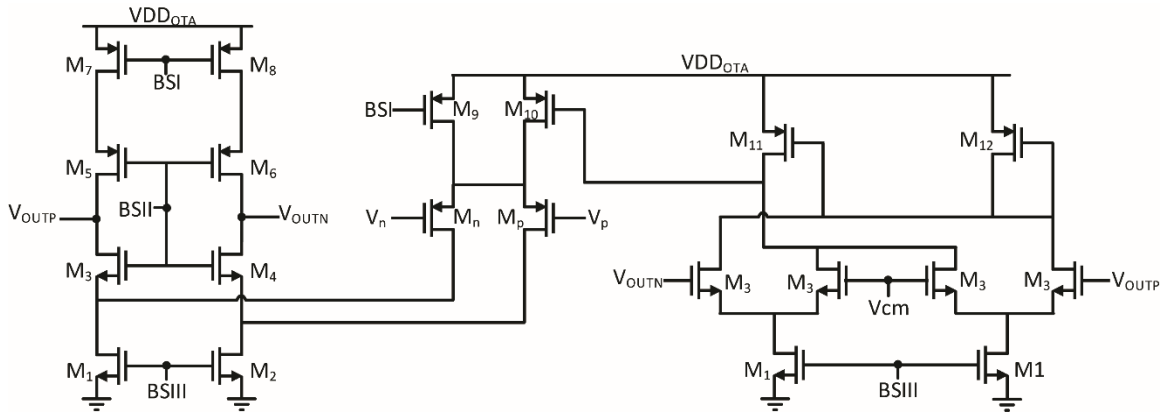
Figure 3.25: Schematic of the fully differential OTA and common mode feedback in the first stage of the recording channel.
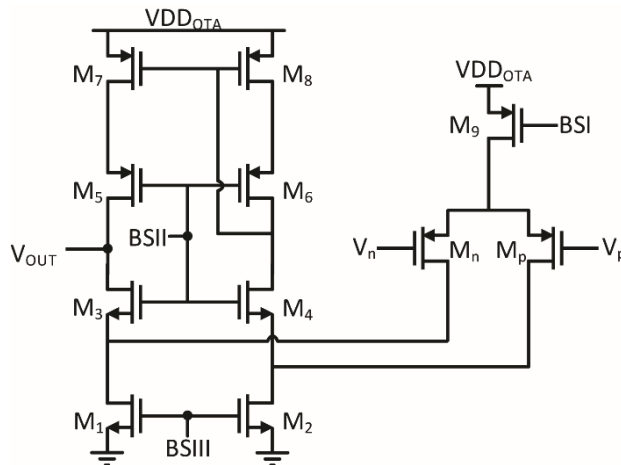
Figure 3.26: Schematic of the single-ended OTA in the second stage of the recording channel.

Table 3.5: Sizing of the transistors in the fully diffrential OTA.

Transistor	M_n	M_p	M_1	M_2	M_3	M_4	M_5
W/L	$\dfrac{4.2\mu}{900n}$	$\dfrac{4.2\mu}{900n}$	$\dfrac{1.8\mu}{900n}$	$\dfrac{1.8\mu}{900n}$	$\dfrac{1.8\mu}{900n}$	$\dfrac{1.8\mu}{900n}$	$\dfrac{4\mu}{900n}$
Transistor	M_6	M_7	M_8	M_9	M_{10}	M_{11}	M_{12}

60

W/L	$\frac{4\mu}{900n}$	$\frac{2.4\mu}{900n}$	$\frac{2.4\mu}{900n}$	$\frac{2.4\mu}{900n}$	$\frac{2.4\mu}{900n}$	$\frac{4.8\mu}{900n}$	$\frac{4.8\mu}{900n}$

Table 3.6: Sizing of the transistors in single-ended OTA.

Transistor	*Mp*	*Mn*	*M₁*	*M₂*	*M₃*	*M₄*	*M₅*	*M₆*	*M₇*	*M₈*	*M₉*
W/L	$\frac{4.2\mu}{900n}$	$\frac{4.2\mu}{900n}$	$\frac{1.8\mu}{900n}$	$\frac{1.8\mu}{900n}$	$\frac{1.8\mu}{900n}$	$\frac{1.8\mu}{900n}$	$\frac{4\mu}{900n}$	$\frac{4\mu}{900n}$	$\frac{2.4\mu}{900n}$	$\frac{2.4\mu}{900n}$	$\frac{4.8\mu}{900n}$
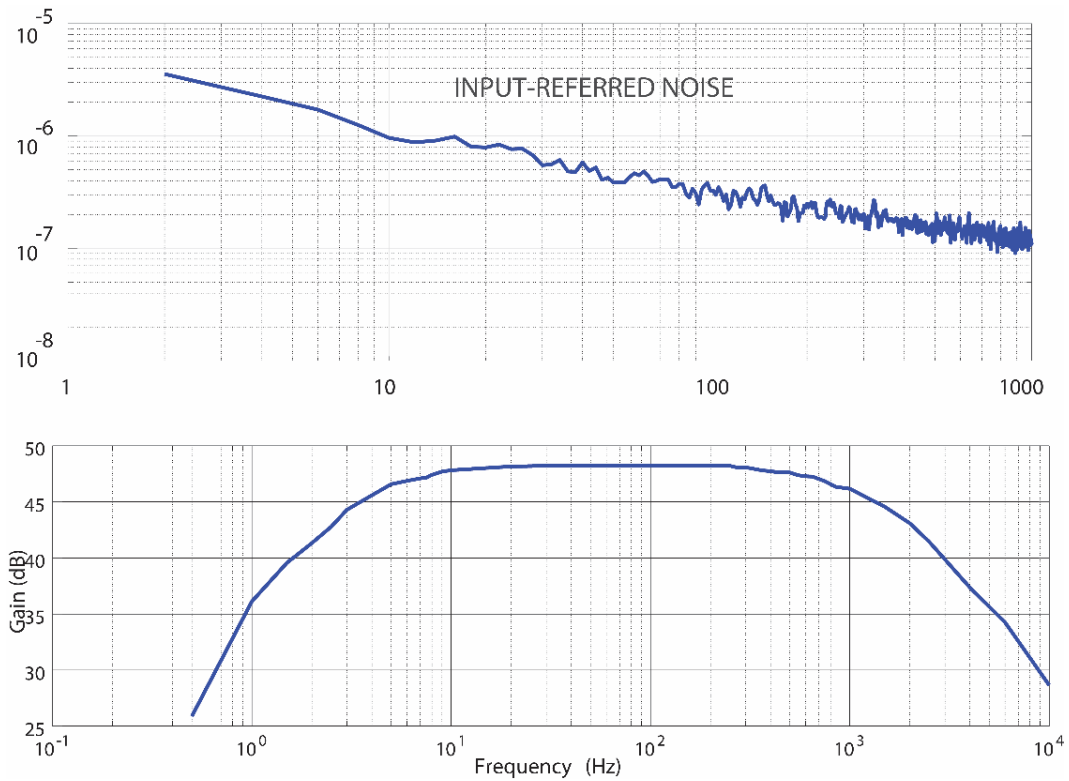
Figure 3.27: Experimentally measured frequency response of the recording channel.
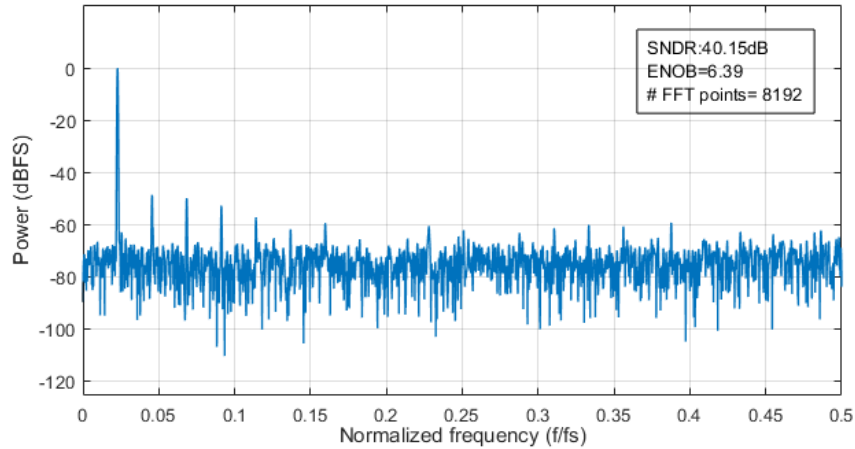
Figure 3.28: Measurement results showing the output PSD of the 8-bit SAR ADC.

3.5 Power management

Brain neural stimulation happens quite infrequently (e.g., at the onset of an epileptic seizure that happens once or a few times a day), which means that for the majority of the time that the device is being used, it is only consuming μW-level power. However, during the optical stimulation, an instantaneous power of up to 33mW (3.3V×10mA) is required. Based on the above, and given the limitation of the inductive power link in terms of the maximum possible (and safe) transfer of energy to the on-chip coil at any moment, an energy storage unit (e.g. a super capacitor) is planned to be integrated with the microchip and μLEDs. Details of this implementation are outside of the scope of this thesis as it is done by another team member. Additionally, while the presented system is capable of generating different lighting patterns with various magnitude and duty cycles, there are other limitations in deciding practical patterns for optical stimulation. The first issue is that each opsin has a special time constant of its own, which means it cannot respond to optical stimulation with

62

frequencies higher than a certain amount. It has been suggested [37] in that the maximum frequency for an effective optogenetic stimulation is 100Hz.

On the other hand, high power consumption of the LEDs results in a considerable amount of heat dissipation, which can easily harm the brain tissue. This introduces a limit on the duty cycle of the lighting pattern in order to make sure the temperature variation does not exceed the safe border, which is an increase of 1°C for brain tissue [7], [38]. Figure 3.29 shows the micrograph of the presented 3×4 mm^2 microchip designed and fabricated in TSMC 130nm CMOS technology. The recording and stimulation channels are highlighted and their corresponding dimensions are annotated. The figure also shows the placement of the coil on the implantable chip. Finally,

Table 3.7 summarize the overall specification of the optical stimulation and recording channel. Finally, in Table 3.8 the proposed design is compared with the state of the art.
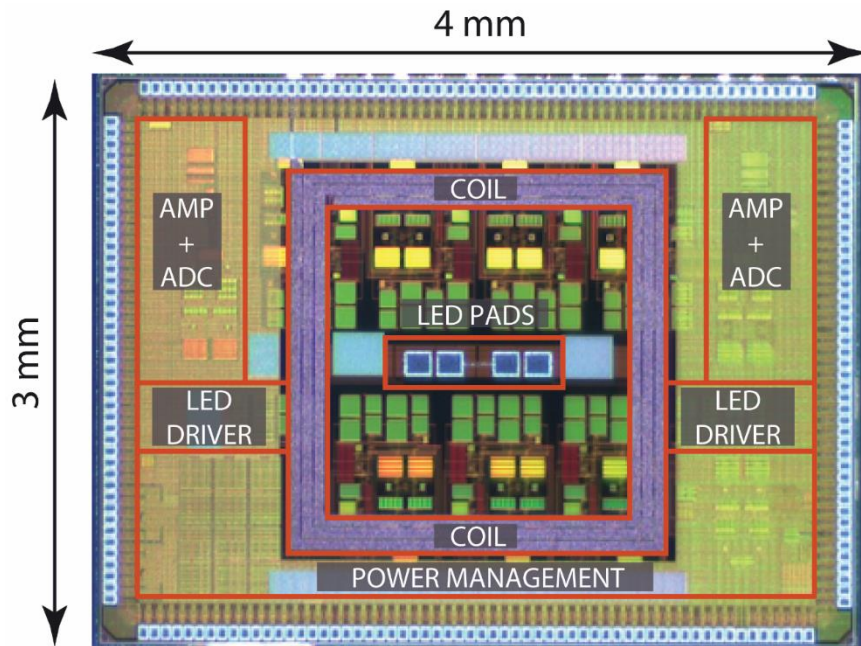
Figure 3.29: The presented SoC micrograph with major blocks on the chip annotated.

Table 3.7: Optical stimulation and electrical recording specification summary.

Overall System	
ASIC area	$12mm^2$
Power with Stimulation	$I_{LED} \times 3.3$
Power w/o Stimulation	$160\mu W$
Optical Stimulation Parameters	
Spatial Resolution	$100 \, \mu m^2$
Irradiance improvement	x30.46
# of channels	2
DAC resolution	3-bits
Gain	850
Stim pattern	Arbitrary
Recording and Digitization Parameters	
# of channels	2
Gain	48.5dB
Bandwidth	3Hz – 1kHz
IRN (1Hz – 1kHz)	$9.98\mu V_{RMS}$
ADC resolution	8 bits
ADC ENOB	6.39

Table 3.8: Comparison with state of the art.

Publication		[15]	[12]	[19]	This Work
Technology		COTS	0.13µm	0.35µm	0.13µm
LED Branch Supply		NA	3.7	5	3.3
Wireless Power		Yes	No	Yes	Yes
Electrical Recording (# of Channels)		No	Yes (10)	No	Yes (2)
ADC		No	ΣΔ (14-bits)	No	SAR (8-bits)
# of Stimulation Channels		1	4	16	2
Light Directivity Enhancement		No	No	Yes	Yes
Optical Stimulation	Max Current	NA	35mA	10mA	15mA
	Current Control	No	Yes (1-bit)	Yes (2-bit)	Yes (3-bit)
	Pattern Control	No	No	No	Yes
Size (mm^3)		10-25	3000	12	6
Weight (mg)		20-50	4900	24	9.5

3.6 Measurement setup

Figure 3.30 illustrate the PCB boards that has been used to characterize the described chip. Both board has been design using the Altium Designer software. Different modes of operation for the PCB can be realized via FPGA codes and changing the positions of the jumpers.

The optical stimulation test was conducted using the packaged version of the CREE TR2227 LED (CLM3A-BKW-CTBVA463 for blue LED and CLM3A-GKW-CWAXA793 for green LED). All the electrical measurements has been conducted based on the measurement setups described in [39].
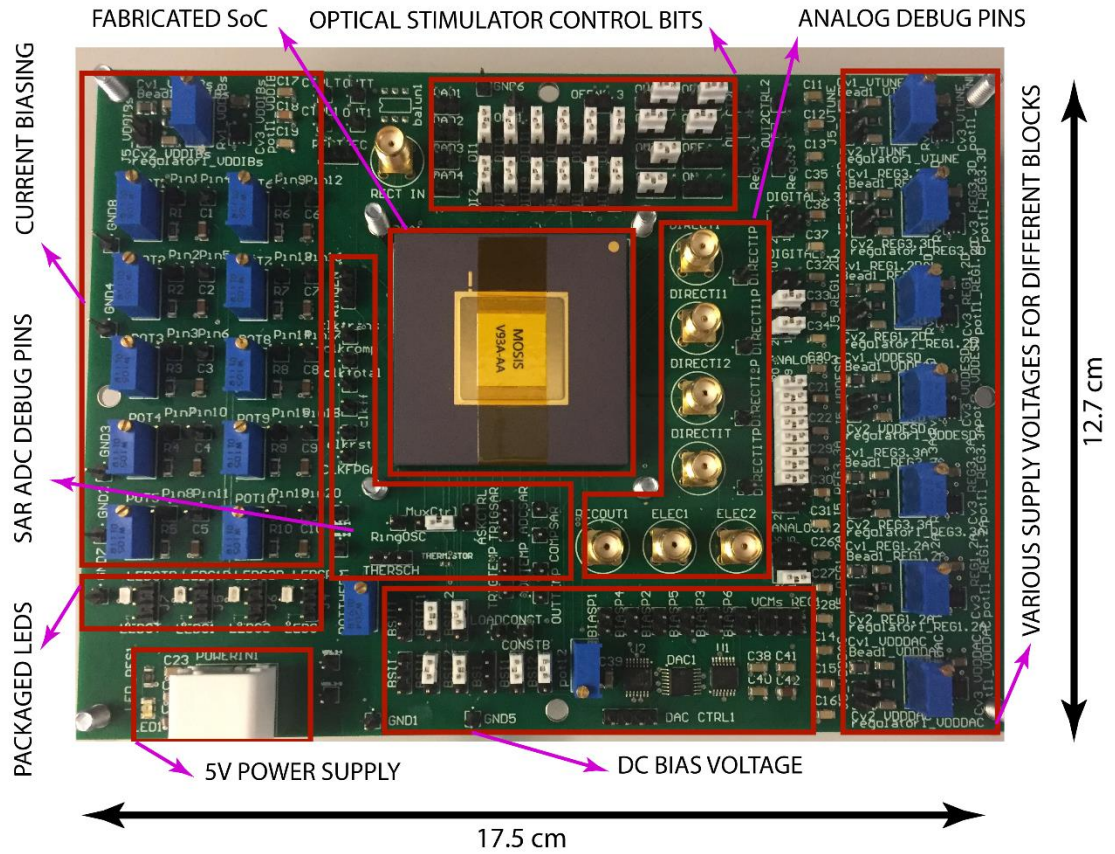
Figure 3.30: Measurement setup used for SoC prototype electrical characterization.

3.7 In Vitro experiments

Figure 3.31 shows the setup of the in vitro experiment, which was design to validate the functionality of the optical stimulator circuitry. We used dynamic Ca^{2+} Imaging method to investigate the channel rhodopsin (hChR2) activity in response to the optical stimulation. In this experiment, transfected Neuro2a cells were incubated in DMEM(-)phenol red with Ca2+ indicators Oregon Green 488 BAPTA-AM Cell Permeant (OGB) (Thermo Fisher

Inc., Mississauga, ON, Canada) for 15 minutes on MekTek plates. Cells were washed with PBS+/+before fresh DMEM(-)phenol red was added.

Cells were imaged using a Zeiss Observer Z1 Spinning Disk Confocal Microscope equipped with live-cell imaging chamber set to 37°C and 5% CO2. Evolve TIRF camera with a Plan-Apochromat 40x/1.3 Oil DIC M27 objective was used to measure the Ca2+signal changes from OGB-BAPTA. The 488nm laser at 10% power intensity was used to monitor OGB-BAPTA channel, while the 568nm laser at 10% power intensity to confirm the expression of channel rhodopsin.

Control (CTRL) plate was used to establish the baseline without the influence of channel rhodopsin, while the test plate was used to determine the change of intracellular calcium levels post stimulation. Cells patches expressing channel rhodopsin were selected using the 568nm laser at 10% power intensity to confirm the expression of channel rhodopsin and monitored over 30 seconds (10s baseline, 10s stimulation, 10s post-stimulation) captured at 200ms intervals. Fluorescence change during baseline was compared to post-stimulated between CTRL cells and channel rhodopsin positive cells were analyzed using the ImageJ plugin time series analyzer V2. Graphs were generated using GraphPad Prism and statistics were generated with IBM SPSS statistics 24.
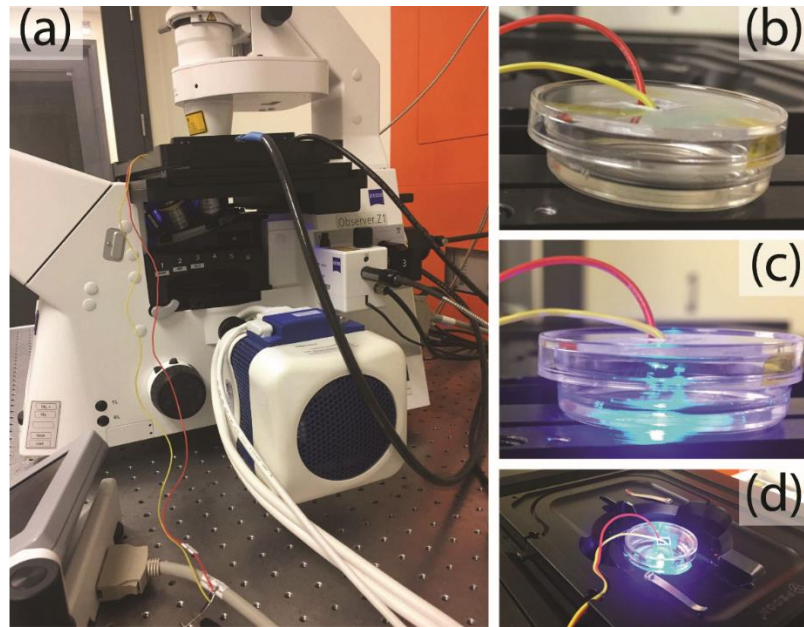
Figure 3.31:In vitro experment setup.

Figure 3.32 illustrate the test result of channel rhodopsin (hChR2) activation in response to optical stimulation, which increase the intracellular calcium levels. Mouse Neuro2a cells were transfected with pAAV-CaMKIIa-hChR2(H134R)-mCherry (red). Figure 3.32 (Top) images from left to right show both channels merged before and after stimulation. The pseudocolour scale indicates the amount of intracellular calcium (blue=min; red=max) (scalebar= 20μm). Figure 3.32 (Bottom, Left) shows the calcium fluorescence changes from the average baseline of Neuro2a cells monitored before and after hChR2 stimulation. The trace shows fluorescence changes (%) over thirty seconds (10s before stimulation, 10s stimulation and 10s post-stimulation). Figure 3.32 (Bottom, right) shows the calcium fluorescence change, which was monitored over a 30s period for control (CTRL) cells (no hChR2; shades of gray) and cells transfected with pAAV-CaMKIIa-hChR2(H134R)-

mCherry (shades of green) (mean±SEM; Mann-Whitney U significance N=5-7; ** p<0.05,

NS= not significant).
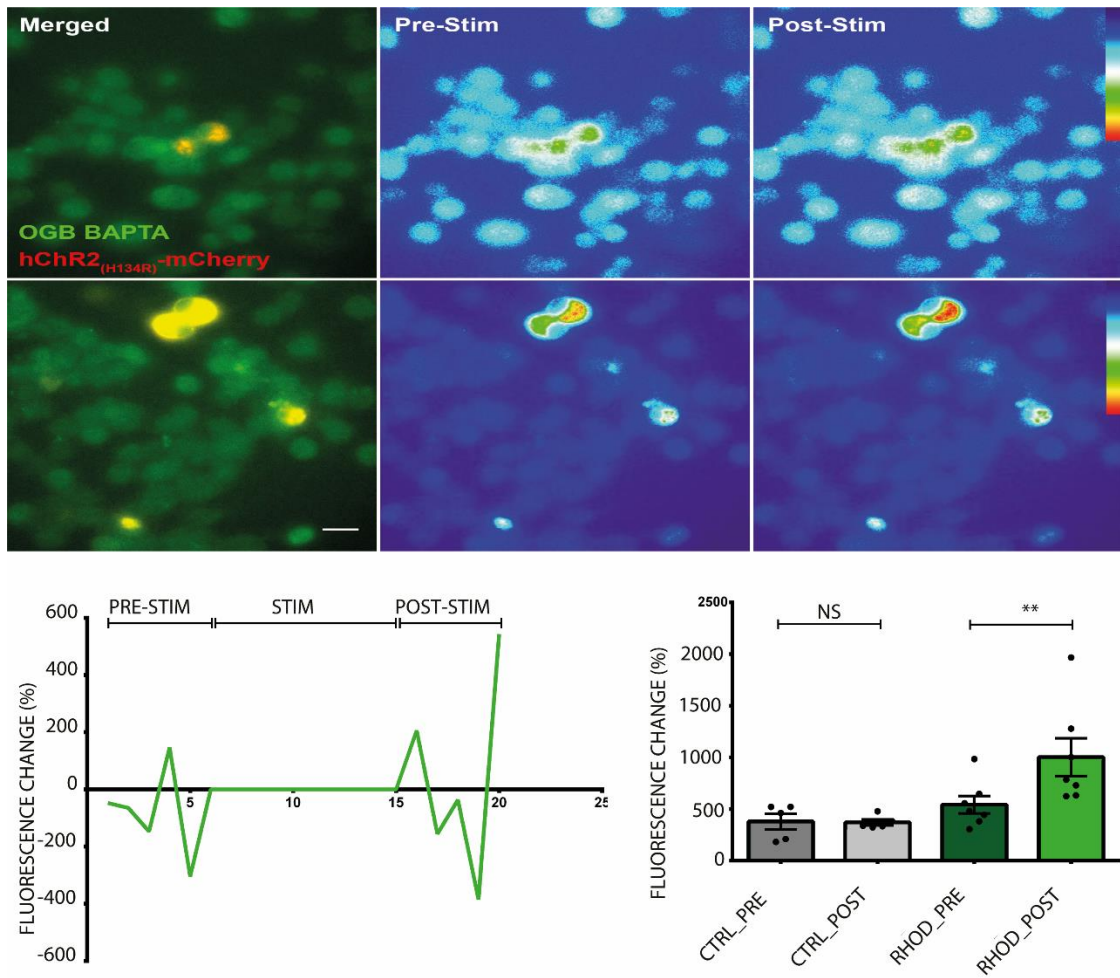
Figure 3.32: Dynamic Ca^{2+} test results.

Chapter 4

Fabrication Process of an Inkjet-Printed SU-8 Polymer-Based Micro-Lens

This chapter presents the fabrication process of the proposed inkjet-printable micro-lens described in chapter 2. Figure 4.1 illustrates the fabrication steps for the micro-lens inkjet-printing process. Substrate preparation is a crucial step prior to the inkjet printing and soft-bake, UV curing and hard-bake are the required steps for solidifying the ink. Details of each step is discussed in details in the rest of this chapter.
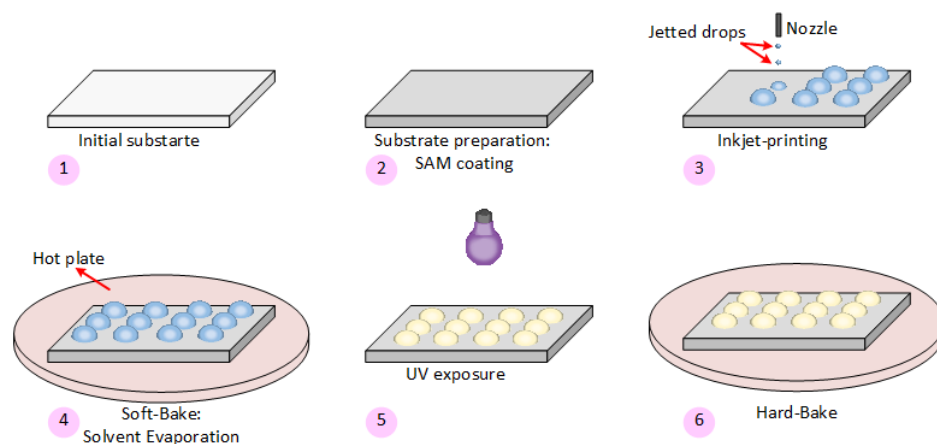
Figure 4.1: Fabrication process of inkjet-printed micro-lenses

4.1 Ink selection for micro-lens fabrication

The first step toward micro-lens fabrication is to choose a proper ink that has the suitable characteristics for the targeted application. The first obvious required feature is high transparency to visible light. Beside this, the ink is required to have a high level of thermal, mechanical, and chemical stability. Biocompatibility is the other important requirement for the proper ink, which is posed by the packaging consideration, since the micro-lens should be in direct contact with the body tissue without any further packaging layers. It should also be compatible with standard inkjet printing equipment or in other words, be jettable.

Based on our comparative review of different types of inks suggested in the literature [40] for micro-lens fabrication, we chose an SU-8-based polymer called InkEpo that meets all the above-mentioned requirements. Table 4.1 summarizes the main physical properties of this material. This information is taken from InkEpo datasheet.

Table 4.1: physical properties of the selected Ink (InkEpo).

	Dyn.Viscosity	*Refractive Index*	*Density*	*Solvent free*	*Photo curing spectral sensitivity*
InkEpo	8.0±0.5 (mPas)	1.47±0.002	1.155±0.002 (gr/cm^3)	No	300-390 (nm)

4.2 Substrate preparation

It is crucial to prepare the substrate prior to the inkjet printing process. Our goal in this project is to print a dome-shape-pattern of the liquid ink on the substrate and solidify it later to fabricate our target micro-lens. Therefore, we require a high contact angle (e.g., > 90 degrees) between the ink and the substrate. To increase the contact angle of our ink on

the surface, we have to make the substrate hydrophobic. Silanization is a general method to change the hydrophobicity of the surface [41]. Silanization forms a densely packed self-assembled monolayer (SAM) of the silane molecules covalently bonded to the target surface [42]. In this work, Trichloro (1H,1H,2H,2H-perfluorooctyl) silane (PFOCTS) is used to decrease the substrate wettability.

4.2.1 Substrate cleaning

Having a clean substrate is a crucial preliminary condition for the silane molecules to form a covalent bond with the surface molecular structure for instance the SiO_2 Lattice in case of a glass substrate. Substrate cleaning is done by washing and sonicating in Isopropanol (IPA) for 20 minutes followed by washing and sonicating with deionized (DI) water for the same amount of time.

It should be noted that all the beakers and tweezers have also undergone the same cleaning process.

4.2.2 Plasma treatment

Plasma treatment is the next surface modification technique to remove impurities and contaminants. This method also functionalizes the target surface for better acceptance of a secondary material to form a coating layer, which is the SAM layer in our case. This step also allows the fabricated and solid micro-lens to be easily removed from the surface, which is a crucial point in our fabrication process. In this recipe, the surface is exposed to oxygen plasma for 1 minute.

4.2.3 Preparation of silane solution

In this recipe, we submerge the target substrate inside a SAM solution. Our required Solution is a 1mM SAM solution with Toluene being the solvent. To achieve this concentration we need 0.04605 gr of the PFOTS in 100 mL of Toluene.

4.2.4 Coating procedure

Exposure to the silane is happening through solution deposition, which involves submerging the clean substrate into the freshly prepared silane solution. For this recipe, the substrate should be submerged inside the solution for 3 hours. During this time, the container should be tightly caped and can be placed in a cabinet. After this time by taking out the substrate and 20 minutes sonication in acetone, our substrate is ready. Figure 4.2 compares the contact angle of our ink on a glass substrate before and after the silanization treatment. Based on the our measurements using side view camera a contact angle of 90° is reliably achieved following this preparation process.
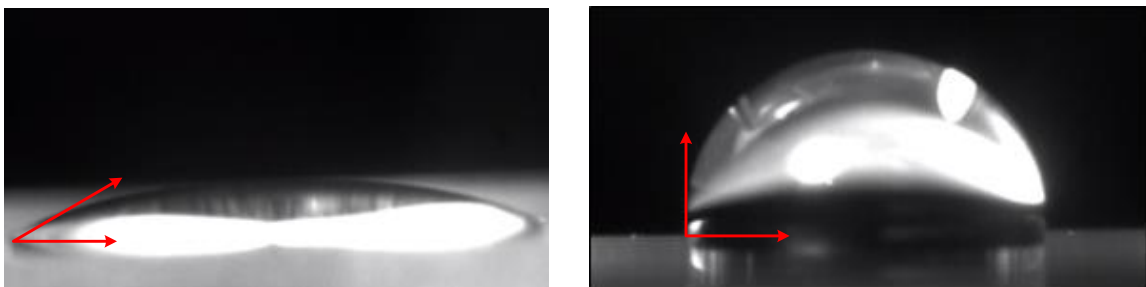
Figure 4.2: Contact angle comparison before (left) and after (right) SAM coating.

4.3 Inkjet printing process

Inkjet printer is a type of digitally-controlled printer suitable for dispensing micro-size droplets to deliver a precise amount of material to the target substrate [43]. Inkjet printers are divided into thermal and piezoelectric [44]. In a thermal inkjet printer, a large current passes through a tiny resistor, which leads to dissipating a considerable amount of heat. The heat vaporizes the ink to create a bubble, and the expansion of this bubble will force some of the ink out of the nozzle. On the other hand, in a piezoelectric inkjet-printer, the vibrations of a piezo crystal, controlled by a voltage signal, push a small amount of ink out of the nozzle.

In this project, we are using a piezo-actuated inkjet printer (MicroFab Technology, USA) with nozzle aperture of 57µm. During the ink selection process, we ensured the jettability of our desired ink by choosing an inkjet compatible ink. We also investigated the jettability of our ink by checking the guideline window presented in [44]. This guideline window presents a systematic approach to investigate ink jettability using capillary number and weber number, which are introduced in Equations (4.1) and (4.2) respectively. In these equations, η, ρ, and σ are the viscosity, density, and surface tension of the ink and d and v are the nozzle diameter and the droplet velocity, respectively. Based on the information provided in the ink datasheet, these dimensionless numbers are calculated as 11 for the weber number and 0.4 for the capillary number, both within the jettable window.

$$Weber\ number, We = \frac{Inertial\ force}{Surface\ tension} = \frac{\rho v^2 d}{\sigma} \qquad \textbf{(4.1)}$$

74

$$Capillary\ number, Ca = \frac{Viscose\ force}{Surface\ tension} = \frac{\eta v}{\sigma} \qquad \textbf{(4.2)}$$

To experimentally validate the jettability and generate the micro-drops, the ink reservoir in the inkjet-printer setup is filled with InkEpo. In order to start the printing process, we have to define the voltage waveform sent to the piezoelectric material. As presented in Figure 4.3, to fully control the shape of this voltage waveform we have to set the values for initial rise time, final rise time, fall time, echo time, dwell time, echo voltage, and dwell voltage. These parameters are determined based on a trial and error procedure to reach a stable jetting condition. For a jetted drop to be considered stable, one single droplet should be formed and it should maintain its physical shape (sphere) for a long time. The satellite drops (any drop other than the main drop) will not affect the jettability as long as their absorption by the main drop during the flight [44]. Table 4.2 reports the optimal parameter for the voltage waveform associated to the stable jetting condition.
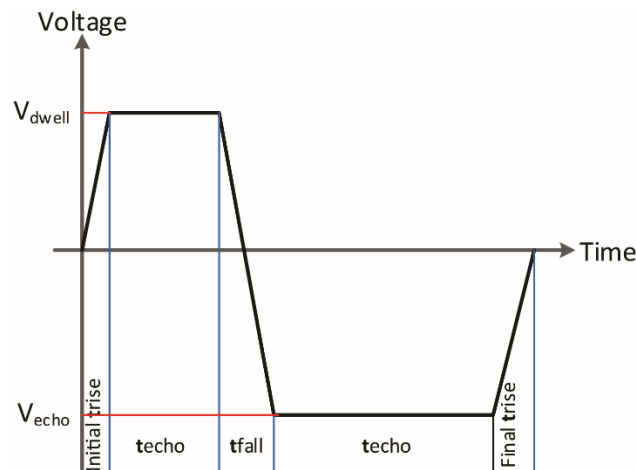
Figure 4.3: Voltage waveform controlling the piezo-actuator.

75

Table 4.2: Optimized parametrs for the voltage waveform controlling the piezo actuator.

V_{dwell}	V_{echo}	Initial t_{rise}	t_{dwell}	t_{fall}	t_{echo}	Final t_{rise}
20 V	-20 V	5µs	44µs	5µs	22µs	5µs

Generation of a stable drop is a complicated process as it is not possible to identify the exact problem in case of an unstable drop. However, some experimentally-validated guidelines could be useful during the trial and error process. First thing to know is that the drop generation occurs during the echo time and the residual oscillation are eliminated during the dwell time [44]. If the voltage waveform parameters are not defined accurately different problems may occur. The first possible problem is that the printer may not be able to generate any drop and since drop generation is the role of the echo time increasing the echo voltage may solve the problem. The other typical problem is generation of stable or unstable satellite drops which is typically related to the dwell time parameters. It is commonly accepted that defining t_{dwell} as $2 \times t_{echo}$ can optimally prevent the satellite drops generation. Figure 4.4 illustrates some cases of satellite generation for non-accurate parameters for the control voltage waveform during my experiments.

Figure 4.4: Some examples of unstable jetting.

Another crucial element that should not be overlooked during the jetting process is cleanliness of the nozzle. Any tiny particle inside the nozzle may jeopardize the printing process completely. Therefore, nozzle cleaning is an essential step before and after each printing experiment.

The properties of the utilized ink dictates the cleaning process. In case of our ink, the cleaning process, include back flush and then flushing the nozzle with first acetone and then IPA. One simple test to make sure the nozzle is fully clean is by checking the output flow of acetone and IPA. The first test to check the cleanness of the nozzle is that the flow should have a straight path outside the nozzle and any deviation from a straight path is an indication of impurity inside the nozzle. The second test is that the flow of the liquid should continue for a short time after releasing the pressure on the syringe. Figure 4.5 presents the generation and flight of the stable drop under the optimal voltage parameters condition.
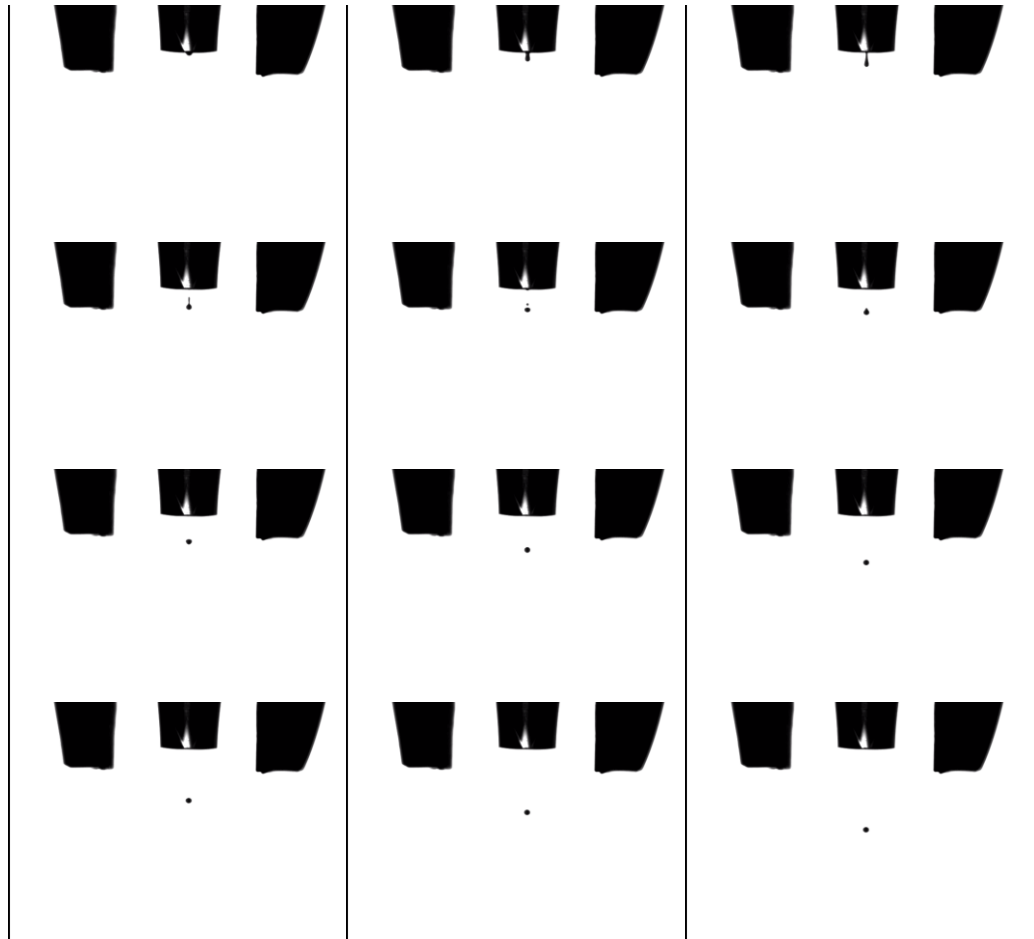
Figure 4.5: Time lapse pictures of stable jet formation and flight.

4.3.1 Ink solidifying process

Being able to generate a stable jet, we can now print a micro-lens by continuous printing on the same spot. Therefore, before attempting to print the optimal lens designed in COMSOL simulation (chapter 2) we tried printing different random-sized lenses to find the effective solidifying process. Solidification process for this ink include three main steps:

1) Soft-bake: placing the sample on a hot plate with temperature of 100°C for 15 minutes.

2) UV exposure: curing under a 400W UV lamp for 4 minutes.

3) Hard-bake: placing the sample on a hot plate with temperature of 100°C for another 15 minutes.

Figure 4.6 shows the fabricated micro-lenses before and after solidification. After the solidification process, the micro-lens color slightly changes and the micro-lenses can be easily detached from the substrate.
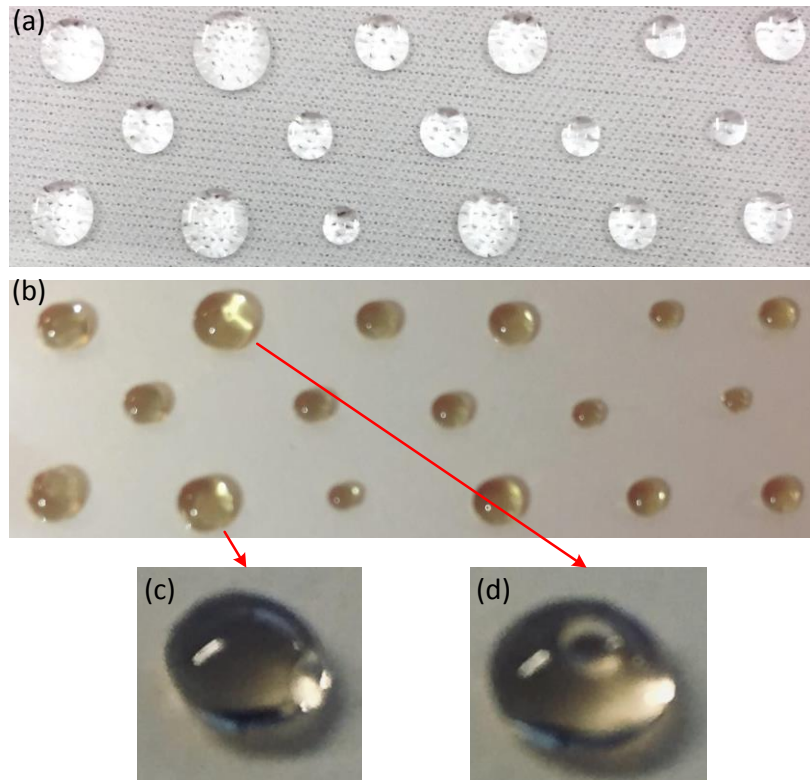
Figure 4.6: Random-size micro lenses (a) before and (b) after solidification.

(c) An example of domeshape micro-lens. (d) An example of micro-lens with coffee-ring effect.

After the UV exposure process, it was visibly noticeable that the larger lenses suffer from the coffee-ring effect. The coffee-ring phenomenon originates from the capillary flow due to the differential evaporation rates across the drop. This force generates a liquid flow from the interior part to the border to substitutes the evaporated liquid at the edges [45]. As presented in Figure 4.7, because of this phenomenon, after the UV exposure, the large micro-lenses have lost their dome-shape and a hole is generated in the middle of the lenses.

Small micro-lens In liquid phase
Diameter<1.5mm

Solidification

Small micro-lens after solidification
No coffee-ring effect

Large micro-lens in liquid phase
Diameter>2.5mm

Solidification

Large micro-lens after solidification
Showing coffee-ring effect
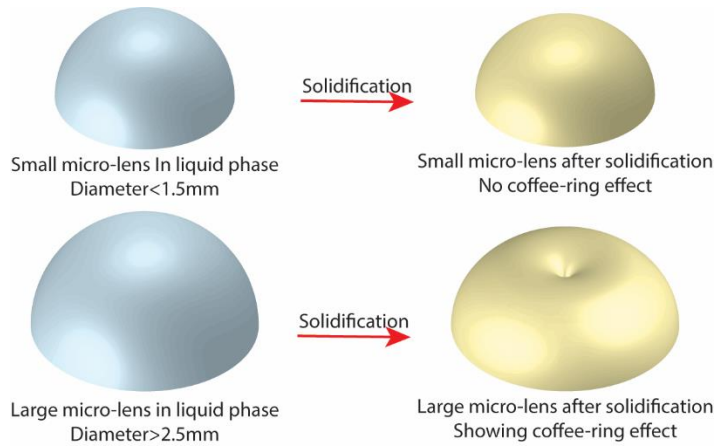
Figure 4.7: Solidification process for small and large micro-lenses.

Occurrence of coffee-ring effect is a function of different factors such as temperature, evaporation time, and the ink material, and therefore, the possibility of coffee-ring effect occurrence is different for each drop. In our experiment, for different sizes of the micro-lens the coffee-ring problem only occurred for drops with a diameter larger than 2mm. Since our optimal lens diameter, based on COMSOL simulation, is in the sub-mm range, there is a very small chance that would suffer from the coffee-ring effect. However, occurrence of coffee-ring effect even in very small scale can be catastrophic for the optical

characterization of the lens. To make sure that it has not caused any deformation in the shape of the small micro-lenses, the post printing profiles are precisely acquired using the profilometer machine, and as presented in Figure 4.8, it is confirmed that the micro-lenses are perfectly dome-shaped.
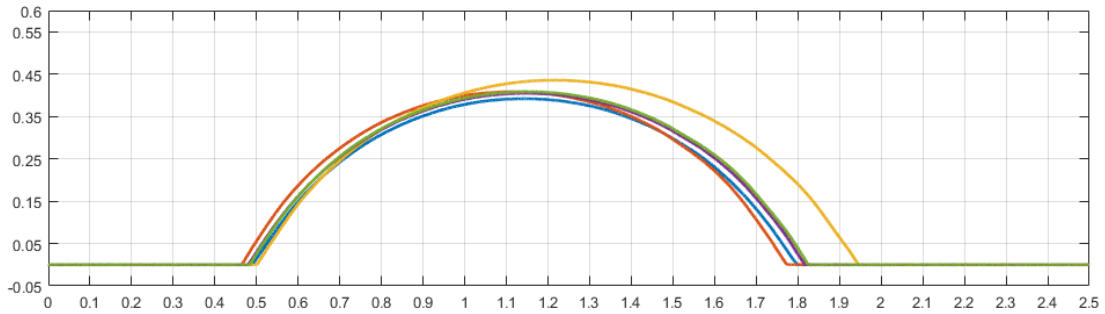
Figure 4.8: Random size lenses profile extracted using the profilometer.

4.3.2 Printing the optimal micro-lens

The first step for printing the optimal lens is to align the tip of the nozzle with our LED to be able to print the lens on top of the LED. Our target micro-lens profile in this stage is a simple dome-shape lens and the inkjet pattern to generate this shape is to eject the drops successively on the center of the µLED.

[46] investigates a chip encapsulation method, such that the chip is placed on a substrate and material suitable for encapsulation is printed on top of the chip in a way that it embraces the chip. We are using the same concept here to print our lens on top of the µLED. This way the micro-lens covers the LED completely and we can accumulate the light emitted from the side-walls of the µLED as well as the top plate. As a result, the only

required parameter in question to generate the pattern for printing our micro-lens is the number of drops.

Therefore, for printing the optimal micro-lens, first the tip of the nozzle should be aligned with the center of the LED and then the optimal number of drops required to generate the optimal micro-lens structure should be calculated.

4.3.2.1 Nozzle alignment with the center of the LED

Alignment process is usually a significant step in any microfabrication procedures. In this project, we need to align the tip of the nozzle with the center of the LED to make sure that a fully symmetrical micro-lens is shaped around the LED.

This type of alignment requires a perpendicular view to the LED, which means placing the camera on top of the substrate with the nozzle in the path. However, the components of the inkjet printer and the nozzle holder itself will block the top view sight of the camera.

Therefore, the alignment process was decided to be done using the side-view camera, simply due to being more practical. The camera should be adjusted in a way that we can get a sight of the nozzle tip and the LED. Then just by adjusting the Y-axis of the chuck, we try to place the LED and the nozzle tip, on the same line. To align the LED and nozzle tip the X-axis should be considered as well. To do so, we can turn the chuck by exactly 90° and adjust the Y-axis in a similar fashion. These two steps will precisely align the tip of the nozzle with the LED center.

4.3.2.2 Calculation of required number of drops

To print any special structure, we have to generate a code for the inkjet-printer, which defines the relative X and Y position of the nozzle tip to the substrate and the number of drops in each position. For our micro-lens which has a dome-shape structure the pattern is only successive drops on the same spot and the spot is defined in the alignment stage which means the relative X and Y position would not change. Therefore, we only need to define the required number of drops. This number is calculated by dividing the volume of the micro-lens in the liquid phase by the volume of a single drop.

As presented in Figure 4.9 defining the volume of a single drop can be done by comparing it with the nozzle tip diameter. In our case, the nozzle tip diameter is 57μm, and the nozzle holder diameter is 625 μm, which results in diameter of 58.76μm for the drop; therefore, the volume of the drop is 106175.364 μm^3.

Figure 4.9: Drop diameter calculation in comparison with nozzle diameter.

Finding the initial volume of the micro-lens right after the printing process is not as straight forward as finding the micro-drop volume. The initial volume of the lens is actually a function of the optimal micro-lens geometry. The COMSOL simulation results for the optimal micro-lens geometry are applicable to the micro-lens in the final state,

which means after solidification. Therefore, by having the final micro-lens volume information we have to calculate the initial volume of the micro-lens in liquid phase. Solvent evaporation during the solidification process is the underlying reason for the difference in the micro-lens volume before and after the solidification process.

The solvent evaporation percentage is a constant parameter for different micro-lens sizes and is dependent the initial ratio of ink and solvent. Since evaporation percentage is a constant parameter for the ink, it can be calculated for a test micro-lens and then we use the acquired information to find the optimal number of drops. Printing a known number of drops provides a fairly precise calculation of the initial volume and the final volume is measured using the profilometer. Next, the evaporation percentage is calculated based on the equation (4.3). It should be noted that the volume of the LED should be subtracted from volume of the target geometry of LED + micro-lens to find the volume of the printed ink before and after solidification.

$$Evaporation\ Percentage = \frac{V_{initial\ lens} - V_{final\ lens}}{V_{initial\ lens} - V_{LED}} \times 100 \qquad \text{(4.3)}$$

Having the Evaporation percentage and volume of the optimal micro-lens in final state, optimal micro-lens volume in liquid phase is calculated. Following this process the required number of drops is 2562 drops and the fabrication process would be printing this many drops on the same position to from a dome-shape micro-lens.

4.4 Optical measurements

Figure 4.10 shows our optical measurement setup, where we used a photo-detector (S121C, Thorlabs) in addition to an optical power meter (PM100D, Thorlabs) to measure the amount of optical power delivered to the photo-detector which is placed in front of the µLED+micro-lens configuration. In order to investigate the micro-lens capability in converging the µLED light, the power meter aperture should be adjustable. Therefore, we used a mountable iris diaphragm (ID25, Thorlabs) between the µLED and the photo-detector to be able to adjust the aperture.

Figure 4.10: Optical measurements setup.

Figure 4.11 presents the measurement result for optical power versus µLED current in range of 1 to 10mA. This measurement is done at a fixed aperture with diameter of 1mm and the LED is placed at 0.5cm distance from the photo detector. The measurements show average improvement of 99.68% in the optical power delivered to the photodetector. Figure 4.12 shows the percentage of improvement in the optical power delivered to the

photo-detector, which stands for the target in our measurement setup, versus the aperture diameter and it shows how the improvement percentage increase with shrinking the aperture area which shows that the micro-lens is successfully converging the LED light. For this measurement, the photodetector is placed at 4cm distance from the µLED.
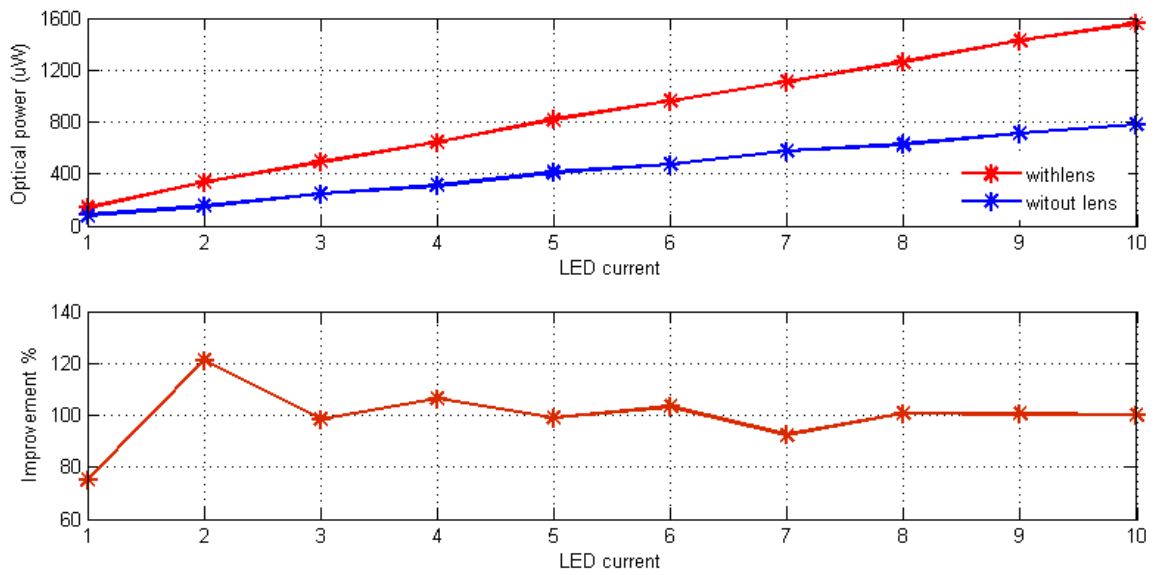
Figure 4.11: Experimentally measured optical power using with and without the micro-lens
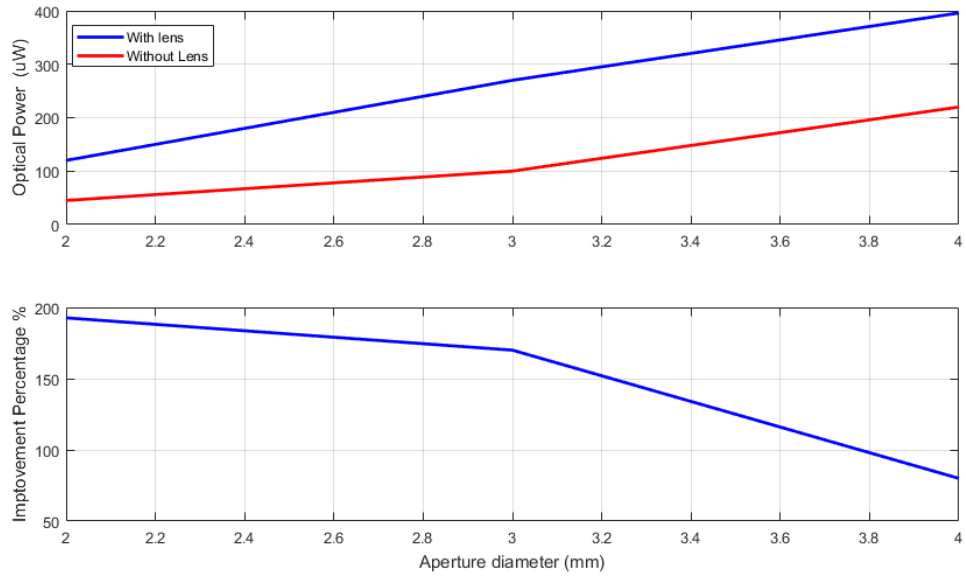
Figure 4.12: Optical power improvement percentage vs aperture diameter.

Chapter 5

Conclusions and Future Directions

5.1 Conclusion

In this work, an integrated SoC for conducting simultaneous dual-channel electrical recording and optical stimulation is presented. Wireless power receiving through an on-chip coil allow the SoC to be fully implantable.

A novel LED driver is presented that can provide currents in range of 1 to 10mA and it exhibits linear performance with headroom voltage as low as 150mV, which is the smallest headroom voltage reported yet. Therefore, we could achieve the highest power efficiency in terms of what percentage of the power drawn from the supply voltage is actually used in the LED. The final design is fabricated as a 3×4 mm^2 microchip using a CMOS 130nm technology.

The proposed method for fabricating a micro-lens on top of the µLED using inkjet-printer for directivity enhancement results in significant improvements in terms of spatial resolution and power efficiency. Optimization process to find optimal configuration for the micro-lenses significantly reduces the required source power (30.5x reduction) to deliver

a specific light intensity to a target tissue, also ensures safety aspects (temperature increase of   <0.1ºc) of the device.

5.2 Future work

5.2.1 SoC improvements

The proposed design should be experimentally validated to insure the functionality of the different blocks. After validating the performance of each of the blocks separately, the next step is to investigate the functionality of the whole system.

For the next generation of this design, since temperature variation is one of the main concerns in optogenetic devices, the next design will be equipped with an on-chip temperature sensor. Besides, in order to wirelessly transmit the data from the recording channels and temperature sensor and receive the controlling signal for the optical stimulation channel, a data transceiver will be implemented on the chip.

5.2.2 Micro-lens improvements

In terms of the micro-lens optimization, various shapes of micro-lenses for different applications can be optimized and implemented. For example, developing a specific structure for our micro-lens, which can direct the output light from both LEDs (Blue and Green) on the same point. This structure would be really useful for experiments that involve step function opsins, since they are responsive to both green and blue LEDs.

5.2.3 Biological experiments

In order to validate the functionality of the design from a neurological perspective, an in vitro experiment is a necessary step. With the proposed LED driver circuit, we can generate various pattern and light intensity for optical stimulation. Therefore, we can experiment the opsins reaction to many different scenarios. The next step after in vitro experiments is to conduct in vivo experiment with freely moving animals, which allows for different types of behavioural studies.

5.2.4 Encapsulation and packaging

Encapsulation and packaging is an important step prior to any in vivo experiment to ensure the safety of placing the device inside the body. The barrier layer should be able to first, protect the device against the chemical material inside the body like the ions and fluids and second, protect the body tissue against the possible toxic components and electrical voltages. It should be noted that the implemented micro-lens is fabricated using a biocompatible ink, since it should be in direct contact with the body tissue and should not be covered with any further encapsulation layers.

Bibliography

[1]   J. Riss, J. Cloyd, J. Gates, and S. Collins, "Benzodiazepines in epilepsy: pharmacology and pharmacokinetics," *Acta Neurol. Scand.*, vol. 118, no. 2, pp. 69–86, Aug. 2008.

[2]   M. S. Steven and A. Pascual-Leone, "Transcranial magnetic stimulation and the human brain: an ethical evaluation," in *Neuroethics*, 2004, pp. 201–212.

[3]   H. Kassiri *et al.*, "Closed-Loop Neurostimulators: A Survey and A Seizure-Predicting Design Example for Intractable Epilepsy Treatment," *IEEE Trans. Biomed. Circuits Syst.*, vol. 11, no. 5, pp. 1026–1040, Oct. 2017.

[4]   B. M. T. Alt *et al.*, "Let There Be Light — Optoprobes for Neural Implants," *Proc. IEEE*, vol. 105, pp. 101–138, 2016.

[5]   S. B. Goncalves, J. F. Ribeiro, A. F. Silva, R. M. Costa, and J. H. Correia, "Design and manufacturing challenges of optogenetic neural interfaces: a review," *J. Neural Eng.*, vol. 14, no. 4, p. 041001, Aug. 2017.

[6]   K. Deisseroth, G. Feng, A. K. Majewska, G. Miesenbock, A. Ting, and M. J. Schnitzer, "Next-Generation Optical Technologies for Illuminating Genetically Targeted Brain Circuits," *J. Neurosci.*, vol. 26, no. 41, pp. 10380–10386, Oct. 2006.

[7]   O. Yizhar, L. E. Fenno, T. J. Davidson, M. Mogri, and K. Deisseroth, "Optogenetics in Neural Systems," *Neuron*, vol. 71, no. 1, pp. 9–34, Jul. 2011.

[8]   D. C. Gadsby, "Ion channels versus ion pumps: the principal difference, in principle.," *Nat. Rev. Mol. Cell Biol.*, vol. 10, no. 5, pp. 344–52, May 2009.

[9]   E. Boyden, F. Zhang, E. Bamberg, … G. N.-N., and undefined 2005, "Millisecond-timescale, genetically targeted optical control of neural activity," *nature.com*.

[10]   M. Filali, W. D. Hutchison, V. N. Palter, A. M. Lozano, and J. O. Dostrovsky, "Stimulation-induced inhibition of neuronal firing in human subthalamic nucleus," *Exp. Brain Res.*, vol. 156, no. 3, pp. 274–281, Jun. 2004.

[11]   A. T. Avestruz *et al.*, "A 5 μw/channel spectral analysis IC for chronic bidirectional brainmachine interfaces," in *IEEE Journal of Solid-State Circuits*, 2008, vol. 43, no. 12, pp. 3006–3024.

[12]   G. Gagnon-Turcotte, M. N. Khiarak, C. Ethier, Y. De Koninck, and B. Gosselin, "A 0.13nm CMOS SoC for Simultaneous Multichannel Optogenetics and Neural Recording," *IEEE J. Solid-State Circuits*, vol. 53, no. 11, pp. 3087–3100, 2018.

[13]   M. Ghovanloo and K. Najafi, "A Compact Large Voltage-Compliance High Output-Impedance Programmable Current Source for Implantable Microstimulators," *IEEE Trans. Biomed. Eng.*, vol. 52, no. 1, pp. 97–105, Jan. 2005.

[14]   G. Shin *et al.*, "Flexible Near-Field Wireless Optoelectronics as Subdermal Implants for Broad Applications in Optogenetics," *Neuron*, vol. 93, no. 3, pp. 509-521.e3, Feb. 2017.

[15]   K. L. Montgomery *et al.*, "Wirelessly powered, fully internal optogenetics for brain, spinal and peripheral circuits in mice," *Nat. Methods*, vol. 12, no. 10, pp. 969–974, 2015.

[16]   S. Nag, P. Lee, R. Herikstad, J. Sng, S. C. Yen, and N. V. Thakor, "Multi-function

optogenetic stimulator and neural amplifier for wirelessly controlled neural interface," in *IEEE Biomedical Circuits and Systems Conference: Engineering for Healthy Minds and Able Bodies, BioCAS 2015 - Proceedings*, 2015.

[17]   R. Ramezani *et al.*, "On-Probe Neural Interface ASIC for Combined Electrical Recording and Optogenetic Stimulation," *IEEE Trans. Biomed. Circuits Syst.*, vol. 12, no. 3, pp. 576–588, 2018.

[18]   J. G. Bernstein *et al.*, "Prosthetic systems for therapeutic optical activation and silencing of genetically-targeted neurons HHS Public Access," *Proc SPIE Int Soc Opt Eng*, vol. 6854, 2008.

[19]   Y. Jia *et al.*, "A mm-sized free-floating wirelessly powered implantable optical stimulating system-on-a-chip," in *Digest of Technical Papers - IEEE International Solid-State Circuits Conference*, 2018, vol. 61, pp. 468–470.

[20]   H. Lee, "A Power-Efficient Wireless Neural Stimulating System with Inductive Power Transmission," *Thesis*, no. May, 2014.

[21]   X. Bi, T. Xie, B. Fan, W. Khan, Y. Guo, and W. Li, "A Flexible, Micro-Lens-Coupled LED Stimulator for Optical Neuromodulation," *IEEE Trans. Biomed. Circuits Syst.*, 2016.

[22]   L. M. Ritter, P. Golshani, K. Takahashi, S. Dufour, T. Valiante, and M. Kokaia, "WONOEP appraisal: Optogenetic tools to suppress seizures and explore the mechanisms of epileptogenesis," *Epilepsia*, vol. 55, no. 11, pp. 1693–1702, 2014.

[23]   J. L.-I. M. Magazine and undefined 2003, "Safety standards for human exposure to

radio frequency radiation and their biological rationale," *ieeexplore.ieee.org*.

[24] T. -i. Kim *et al.*, "Injectable, Cellular-Scale Optoelectronics with Applications for Wireless Optogenetics," *Science (80-.).*, 2013.

[25] N. McAlinden *et al.*, "Thermal and optical characterization of micro-LED probes for in vivo optogenetic neural stimulation.," *Opt. Lett.*, vol. 38, no. 6, pp. 992–4, Mar. 2013.

[26] M. J. Gallagher, "How deactivating an inhibitor causes absence epilepsy: Validation of a noble lie," *Epilepsy Curr.*, vol. 13, no. 1, pp. 38–41, 2013.

[27] M. J. Gallagher, "How Deactivating an Inhibitor Causes Absence Epilepsy: Validation of a Noble Lie," *Epilepsy Curr.*, vol. 13, no. 1, pp. 38–41, Jan. 2013.

[28] D. Brinks, Y. Adam, S. Kheifets, and A. E. Cohen, "Painting with Rainbows: Patterning Light in Space, Time, and Wavelength for Multiphoton Optogenetic Sensing and Control," *Acc. Chem. Res.*, vol. 49, no. 11, pp. 2518–2526, 2016.

[29] V. J. Cadarso *et al.*, "Microlenses with defined contour shapes," *Opt. Express*, vol. 19, no. 19, p. 18665, 2011.

[30] M. Lyons, N. Harrison, G. Brewer, S. Robinson, R. Sanders, and D. Upton, "Introduction to Biological Psychology," in *Biological Psychology*, W.C. Brown, 2017, pp. 1–9.

[31] K. Paralikar *et al.*, "An implantable optical stimulation delivery system for actuating an excitable biosubstrate," in *IEEE Journal of Solid-State Circuits*, 2011, vol. 46, no. 1, pp. 321–332.

[32] M. Quarantelli, M. Poles, M. Pasotti, and P. Rolandi, "A high compliance CMOS current source for low voltage applications," in *Proceedings of the 2003 International Symposium on Circuits and Systems, 2003. ISCAS '03.*, vol. 1, pp. I-425-I–428.

[33] M. H. Maghami, A. M. Sodagar, and M. Sawan, "Analysis and design of a high-compliance ultra-high output resistance current mirror employing positive shunt feedback," *Int. J. Circuit Theory Appl.*, vol. 43, no. 12, pp. 1935–1952, Dec. 2015.

[34] R. R. Harrison and C. Charles, "A low-power low-noise CMOS amplifier for neural recording applications," *IEEE J. Solid-State Circuits*, 2003.

[35] K. Abdelhalim, L. Kokarovtseva, J. L. Perez Velazquez, and R. Genov, "915-MHz FSK/OOK wireless neural recording soc with 64 mixed-signal fir filters," *IEEE J. Solid-State Circuits*, vol. 48, no. 10, pp. 2478–2493, Oct. 2013.

[36] J. Wang *et al.*, "Integrated device for combined optical neuromodulation and electrical recording for chronic in vivo applications," *J. Neural Eng.*, vol. 9, no. 1, p. 016001, Feb. 2012.

[37] E. Krook-Magnuson, G. G. Szabo, C. Armstrong, M. Oijala, and I. Soltesz, "Cerebellar Directed Optogenetic Intervention Inhibits Spontaneous Hippocampal Seizures in a Mouse Model of Temporal Lobe Epilepsy," *eNeuro*, vol. 1, no. 1, Nov. 2014.

[38] K. L. Montgomery *et al.*, "Wirelessly powered, fully internal optogenetics for brain, spinal and peripheral circuits in mice," *Nat. Methods*, 2015.

[39] R. R. Harrison, "Integrated Biopotential Amplifiers : Architecture , Performance , and Testing." tutorial. IEEE BioCAS 2011.

[40] A. Voigt *et al.*, "New inks for the direct drop-on-demand fabrication of polymer lenses," *Microelectron. Eng.*, vol. 88, no. 8, pp. 2174–2179, 2011.

[41] O. U. Nimittrakoolchai and S. Supothina, "Deposition of organic-based superhydrophobic films for anti-adhesion and self-cleaning applications," *J. Eur. Ceram. Soc.*, vol. 28, no. 5, pp. 947–952, 2008.

[42] M. Lessel *et al.*, "Self-assembled silane monolayers: An efficient step-by-step recipe for high-quality, low energy surfaces," *Surf. Interface Anal.*, vol. 47, no. 5, pp. 557–564, 2015.

[43] W. R. S. Baxter, S. Temple, J. Morgan, G. D. Martin, I. M. Hutchings, and J. R. Castrejon-Pita, "Future, Opportunities and Challenges of Inkjet Technologies," *At. Sprays*, vol. 23, no. 6, pp. 541–565, 2013.

[44] H. C. Nallan, J. A. Sadie, R. Kitsomboonloha, S. K. Volkman, and V. Subramanian, "Systematic design of jettable nanoparticle-based inkjet inks: Rheology, acoustics, and jettability," *Langmuir*, vol. 30, no. 44, pp. 13470–13477, 2014.

[45] R. D. Deegan, O. Bakajin, T. F. Dupont, G. Huber, S. R. Nagel, and T. A. Witten, "Capillary flow as the cause of ring stains from dried liquid drops," *Nature*, vol. 389, no. 6653, pp. 827–829, Oct. 1997.

[46] V. J. Cadarso, L. Jacot-Descombes, J. Brugger, M. Mastrangeli, and M. R. Gullo, "Inkjet printed SU-8 hemispherical microcapsules and silicon chip embedding,"

Micro & Nano Lett., vol. 8, no. 10, pp. 633–636, 2013.